Capturing sclera anisotropy using direct collagen fiber models: Linking microstructure to macroscopic mechanical properties.

Fengting Ji[1, 3, †], Xuehuan He[1, †], Frederick Sebastian[4], Mohammad R. Islam[1,2], Hannah Schilpp[1], Bingrui Wang[1], Yi Hua[1,5], Rouzbeh Amini[4,6], Ian A. Sigal [1, 3 *]

[1] Department of Ophthalmology, University of Pittsburgh, Pittsburgh, PA
[2] Department of Mechanical Engineering, University of Texas Rio Grande Valley, Edinburg, TX
[3] Department of Bioengineering, University of Pittsburgh, Pittsburgh, PA
[4] Department of Bioengineering, Northeastern University, Boston, MA
[5] Department of Biomedical Engineering, University of Mississippi, University, MS
[6] Department of Mechanical and Industrial Engineering, Northeastern University, Boston, MA

Short Title: Modeling sclera fibrous anisotropy

† Both F. Ji and X. He should be considered first authors

* **Correspondence**:
Ian A. Sigal, Ph.D.
Laboratory of Ocular Biomechanics
Department of Ophthalmology, University of Pittsburgh Medical Center,
1622 Locust St. Rm 7.382, Pittsburgh, PA, USA. 15219
Email: ian@OcularBiomechanics.com
www.OcularBiomechanics.org

Keywords: Collagen, Microstructure, Sclera, Finite element modeling, Biomechanics

Disclosures: F. Ji, None; M.R. Islam, None; F. Sebastian, None; H. Schilpp, None; B. Wang None; Y. Hua, None; R. Amini, None; I.A. Sigal, None.

Funding: This work was supported in part by the National Institutes of Health R01-EY023966, P30-EY008098, and T32-EY017271 (Betare thesda, MD). The Eye and Ear Foundation (Pittsburgh, PA). Research to Prevent Blindness (unrestricted grant to UPMC ophthalmology, and Stein innovation award to Sigal IA).

Abstract

Collagen fibers are essential to the mechanical behavior of soft tissues, including sclera. Conventional models often represent these fibers statistically, potentially missing crucial aspects of their role in tissue behavior. In this study, we expand on a direct fiber modeling approach that we recently presented based on explicitly representing the sclera long, interwoven fiber bundles. Specifically, our goal was to capture specimen-specific 3D fiber architecture and anisotropic mechanics of four ovine sclera samples (superior from Eye-1, temporal and superior from Eye-2, and temporal from Eye-3), each tested under five conditions: equibiaxial (1:1) and four non-equibiaxial (1:0.75, 0.75:1, 1:0.5, and 0.5:1). Fiber architecture was extracted using polarized light microscopy and reconstructed model fiber orientations agreed well with the histological information (adjusted $R^2 > 0.89$). Material parameters were determined via inverse fitting to the equibiaxial tests. Remarkably, the parameters obtained from equibiaxial fitting also accurately predicted the mechanical response of the same sample under all four non-equibiaxial conditions. This indicates that the models inherently captured tissue anisotropy through its fiber structure, unlike conventional continuum models which require simultaneous multi-condition fitting. Our findings support direct fiber modeling as a promising tool approach for linking tissue fibrous structure and macroscopic mechanical behavior.

1. Introduction

Biomechanical and mechanobiological analyses are critical tools for understanding the function and dysfunction of ocular tissues (Amini and Barocas 2009; Bellezza et al. 2000; Ethier et al. 2004; Girard et al. 2015; Nguyen and Ethier 2015; Roberts and Liu 2017). In particular, the biomechanics of the corneoscleral shell play a significant role in the pathophysiology of visually impairing disorders such as glaucoma and myopia (Bianco et al. 2024; Feola et al. 2016; Grytz et al. 2020; Midgett et al. 2020; Newson and El-Sheikh 2006). As with many other soft tissues in the body, collagen fibers are the primary load-bearing component of the sclera, providing structural integrity and mechanical strength to the tissue under various physiological and pathological conditions(Boote et al. 2020; Girard et al. 2009b; Grytz et al. 2014; Jan et al. 2017a; Pijanka et al. 2012). Hence, it is important to identify the biomechanical role of scleral collagen fibers, and how their behavior relates to physiology and pathology (Coudrillier et al. 2012; Ethier et al. 2004; Pijanka et al. 2012; Rada et al. 2006). In recent years, computational modeling has emerged as a key approach to study the relationship between scleral fiber structure and its biomechanical response, mainly because of the difficulty in accessing the eye, especially the posterior pole, (Girard et al. 2009a; Grytz et al. 2014; Kollech et al. 2019; Pijanka et al. 2015; Voorhees et al. 2018; Whitford et al. 2016; Zhou et al. 2019).

In the field of collagenous tissue modeling, two predominant approaches are often employed: phenomenological models (Bellini et al. 2011; Humphrey 2003; Khoiy et al. 2018b; Taber 2009) and structurally faithful models (De Jesus et al. 2016; Lanir 1983; Mahutga et al. 2023; Taber 2009; Zhang et al. 2016). Phenomenological models, while capable of predicting large-scale tissue-level deformations, fall short in providing insights into the mechanical environments at the meso-scale. This is not a surprise or necessarily a failure given that, by construction, the models are intended to work at larger scales. However, this limitation hampers their utility in studying the mechanobiology of the extracellular matrix, particularly collagen.

Structurally faithful models offer the possibility of a more nuanced description to soft tissue mechanics at smaller scales. For instance, Ragupathy and Barocas developed a structural model that represented soft tissue mechanics as the sum of fiber contributions across various orientations (Raghupathy and Barocas 2009). They formulated a closed-form analytic solution for the integral describing the overall resultant stress of fibrous tissues, using a von Mises fiber orientation distribution and an exponential fiber stress-strain relationship. Similarly, Fata et al. employed a structural-based model to study postnatal growth in ovine pulmonary arteries (Fata

et al. 2014). Amini and colleagues demonstrated how collagen fibers deform in the clinically relevant deformation of the glenohumeral capsule, using a purely kinematic approach without solving stress balance equations (Amini et al. 2014). They utilized an in-plane convective curvilinear coordinate system to capture the fiber deformation. While these studies provided insights into changes in overall collagen fiber distributions, the fibers were not treated as discrete load-bearing entities. Such an approach limits the structural insights solely to changes in overall fiber distribution without offering specific details about individual fiber bundles.

Another important consideration regarding the abovementioned studies is that they assumed affine deformations —meaning that the local deformation of fibers is assumed to directly follow the global tissue deformation—which may not always accurately represent collagenous tissue behavior. Conversely, non-affine deformations occur when fibers deform differently from the overall tissue, due to local microstructural variations, interactions, or constraints (Chandran and Barocas 2006; Lee et al. 2022). To address non-affine deformations, multi-scale approaches have been employed to connect tissue-level stress with fiber-level stress and deformation through volume averaging methods (Aghvami et al. 2016; Hadi et al. 2012; Mahutga et al. 2023; Pakzadmanesh et al. 2024; Stylianopoulos and Barocas 2007). These models, however, often rely on representative volume elements (RVE) and tend to overlook key characteristics of fibrous constructions, such as fiber interweaving. This omission can limit the accuracy of these models in capturing the full complexity of fibrous tissue behavior (Wang et al. 2020). Compared to RVE-based approaches, the direct fiber modeling framework can naturally represent long-range strain transmission through interwoven fibers, as recently demonstrated in (He et al. 2024).

In the case of sclera and optic nerve, accurately incorporating fiber characteristics at the microscale is likely crucial for correct prediction of the biomechanical effects at the cellular and axonal scales (Lee et al. 2022).

With the intent to improve the ability to model fibrous sclera, we recently introduced a direct fiber modeling technique (Ji et al. 2023a). In this approach, fiber families, or bundles, were reconstructed and simulated using detailed, specimen-specific fiber architectures derived from histological analysis through polarized light microscopy (PLM) (Jan et al. 2015). In doing so, the models account for fiber interweaving, fiber-fiber interactions, and long fibers. We demonstrated the capabilities of the *direct fiber* modeling approach in two studies with different scales. In the first study, we reconstructed a model of a small sample of temporal sclera, and then used an inverse fitting approach to match experimental equi-biaxial stress-strain data from the literature, simultaneously capturing the behavior in both radial and circumferential directions (Ji et al. 2023a).

In the second study, we applied the direct fiber modeling approach to reconstruct a model of the optic nerve head (ONH) and the adjacent tissues, a substantially larger region than the sclera sample (Islam et al. 2024). Due to the size and complexity of the region being modeled, we adjusted our approach to utilizing histological data for reconstructing the model. Specifically, we prioritized the modeling of larger fiber bundles, 200–400 μm thick, rather than smaller fibers. Despite employing linear mechanical properties for the tissue, the model effectively captured the overall behavior of the optic nerve head under inflation, including the emergence of nonlinear characteristics (Islam et al. 2024). Subsequently, we demonstrated that the direct fiber model outperforms the conventional continuum model in capturing both the large-scale tissue strain pattern and the small-scale fiber strain in the sclera region of the ONH (He et al. 2024). While both studies demonstrated the potential of the direct fiber modeling approach, they had several important limitations. Firstly, the histological data and mechanical response data were obtained from different specimens. Specifically, in the first study, the histological data were collected from an ovine eye, whereas the mechanical response data came from a porcine eye. In the second study, both sets of data were derived from the porcine ONH but from different porcine specimens. Furthermore, only a single posterior sclera sample was analyzed, so it was not possible to confirm that the method can consistently capture specimen-specific information. Finally, previous tests of the model were limited to equi-biaxial loading conditions, which do not fully account for the more complex, anisotropic forces that the sclera may encounter in physiological conditions. (Boote et al. 2020).

Our goal in this study was to build on the promise of the studies mentioned above and continue the development and evaluation of the direct fiber modeling of sclera. Specifically, we set a much more challenging objective by requiring that the models capture specimen-specific 3D fiber architecture and experimental anisotropic mechanics of scleral samples obtained from distinct anatomical locations (superior quadrant of Eye-1, temporal and superior quadrants of Eye-2, and temporal quadrant of Eye-3). In addition, we expanded the mechanical loading protocols, moving from only equi-biaxial tests to a set of five tests including equi-biaxial and four non-equi-biaxial tests, thereby covering a broader range of sample behavior and strain energy field.

We show that the direct fiber modeling approach effectively captured the non-linear and anisotropic responses unique to each sample. Unlike phenomenological models, which often rely on simultaneously fitting all biaxial testing protocols to the analytical model (Bellini et al. 2011; Geest et al. 2006), the direct fiber modeling approach demonstrated impressive predictive capabilities. By fitting the model parameters using only one mechanical testing protocol, we were

able to reliably predict responses under other loading conditions. We anticipate that this novel direct fiber modeling approach for the sclera will advance our understanding of the biomechanics and mechanobiology of collagen both in healthy and in diseased eyes. Moreover, we expect this approach to be valuable for modeling other soft tissues or tissue-replacement biomaterials.

2. Methods

This section is organized into three parts: First, biaxial mechanical testing was conducted on healthy sheep posterior pole samples to obtain their stress-strain responses under five loading protocols. Second, the same samples used for mechanical testing were fixed and sectioned, and the sections imaged using PLM. The PLM images were used to build specimen-specific direct fiber models with the fiber orientation data. Each direct fiber model consisted of a fibrous component embedded in a matrix representing the non-collagenous components. Third, each combined fiber and matrix model was used in an inverse fitting optimization process to match the simulated stress-strain behaviors with experimental data acquired under equi-biaxial testing of the same sample. The inverse process produced specimen-specific fiber material properties and pre-stretching strains.

Image processing was done using MATLAB v2020 (MathWorks, Natick, MA, USA) and FIJI, which is a distribution of ImageJ (FIJI) (Preibisch et al. 2009; Schindelin et al. 2012). Modeling was done in Abaqus 2020X (Dassault Systemes Simulia Corp., Providence, RI, 171 USA). Customized code and the GIBBON toolbox (Moerman 2018) for MATLAB v2020 (MathWorks, Natick, MA, USA) were used for model pre/post-processing and inverse fitting.

2.1 Biaxial mechanical testing

The experimental procedures were conducted according to a well-established methodology previously described (Amini Khoiy and Amini 2016; Clarin et al. 2023; Khoiy et al. 2018a; Salinas et al. 2020; Thomas et al. 2019). The study was conducted in accordance with the tenets of the Declaration of Helsinki and the statement for the use of animals in ophthalmic and vision research of the Association of Research in Vision and Ophthalmology. Three fresh ovine eyes were obtained from a local slaughterhouse within 24 hours postmortem and immediately transferred to the laboratory at Northeastern University in a cold isotonic phosphate buffer saline (PBS) solution. Upon arrival, two posterior sclera samples measuring 11mm x 11mm were carefully excised from both temporal and superior quadrants, approximately 2 to 3 mm away from the sclera canal (Figure 1 A). For the purpose of optical tracking and tissue deformation/strain analysis, four submillimeter glass markers were affixed to the surface of each sample.

The sample was then mounted onto the biaxial testing equipment using fishhooks, with the loading axes aligned with the circumferential and radial directions of the sample (Figure 1 B and C). As demonstrated in our previous studies, to prevent alterations in mechanical response, the samples were continuously submerged in isotonic PBS solution throughout the experiment

(Salinas et al. 2019; Salinas et al. 2022). A 0.5 g tare load was initially applied to gently flatten the sample and remove slack without introducing significant pre-stretch. This empirically selected value ensured a consistent, low-strain reference configuration for all samples (Salinas et al. 2019; Salinas et al. 2022). Subsequently, each sample was subjected to biaxial stress control and underwent five distinct loading protocols (Table 1). Each loading protocol consisted of ten 20-second cycles. The first nine cycles served as a preconditioning phase, while data from the last loading cycle were used for subsequent analysis. Based on preliminary tests, a maximum stress level of 150kPa was applied, as it allowed the sample to maintain sample shape without incurring damage. Once the stress-strain data were obtained, the samples were carefully unmounted from the biaxial testing equipment and immersion fixed in 10% formalin for 24 hours. We chose formalin because it has been shown to cause only minimal changes in the shape or size of ocular tissues (Tran et al. 2017).

Temporal and superior samples from three eyes produced six samples. Two of the samples (temporal from Eye-1 and superior from Eye-3) were excluded from further analysis because of tissue damage incurred during the experimental procedures. Hence, the rest of the analysis is based on stress-strain responses from four samples. More details regarding these samples can be found in Table 2.

At the initial stages of the loading tests, the experimental stress-strain data exhibited relatively high noise and variability compared with more stable later steps. These points were excluded from the inverse fitting process. We applied a moving average smoothing algorithm to reduce the noise in the rest of the stress-strain curves (Chang et al. 2015). For the rest of the analysis, we used the experimental data after smoothing.

2.2 Histology, polarized light microscopy and image post-processing

Following the fixation process, the samples were cryo-sectioned into 20 μm-thick slices (Figure 2). To be able to reconstruct accurately the 3D architecture of the samples, we used a process involving both coronal sections (parallel to the surface of the sample) and sagittal sections (perpendicular to the surface sample). For coronal sections, serial sectioning was performed at the center of the sample, every section was collected starting when there was visible sclera and stopping when the sclera was no longer visible. The number of sections collected varied among the different samples because of their different thicknesses and exact orientation, and the specific quantities are detailed in Table 2. To improve the ability of the reconstructions matching the architecture of each sample, for sagittal sections, two slabs from the edge of the square-shaped sample were obtained. In this way we were able to acquire high resolution coronal

data from the core of the tested sample, and high-resolution transverse data at the core edge. Coronal and sagittal sections approximate two orthogonal views of the collagen structure, providing information on the three-dimensional organization of the fibers.

All sections were imaged with PLM as described before (Jan et al. 2015; Jan et al. 2017b). Briefly, two polarized filters (Hoya, Tokyo, Japan) were used, one a polarizer and the other an analyzer, to collect images at four filter orientations 45° apart. We have shown that this protocol produces excellent fiber orientation data for ocular tissue samples (Jan et al. 2015). The images were all captured using an Olympus MVX10 microscope (1× magnification setting, 6.84 μm/pixel).

PLM images were processed to derive the in-plane collagen orientation at each pixel (in Cartesian coordinates) and a parameter that we referred to as “energy”(Yang et al. 2018). In our PLM analysis, “energy” quantifies the strength of the birefringence signal across different polarizer angles. It is highest in regions where collagen fibers are well-aligned within the imaging plane, and lower in areas with weak signal, such as those lacking collagen or where fibers are oriented out-of-plane. This parameter is used to weight pixel contributions when computing orientation distributions, ensuring that the final histograms reflect meaningful structural information. Following the processing of PLM images, all images obtained from a single sample were sequentially stacked and registered based on the sharp edges (Gogola et al. 2018b). After registration, the original images underwent reprocessing to obtain "corrected" orientation angles that are consistent across all the sections.

To focus on a specific area for subsequent construction of the direct fiber model, we selected a square-shaped block positioned at the center of the coronal sections. The dimensions of this selected block were 4.1x4.1mm (Figure 3A). However, due to the irregular shape of the tissue and the folds caused during tissue sectioning, the stack of cropped blocks exhibited variations in thickness (Figure 3C). In order to facilitate fiber tracing for the construction of the direct fiber model, we implemented a linear interpolation algorithm, as described by Akima (Akima 1970; Akima 1974). The interpolation algorithm was employed to interpolate angle and energy values at each location in-depth within the stack, thereby converting the inconsistent thicknesses into a uniform value. As a result of this interpolation, the image stack was transformed into a uniform and regular block (Figure 3D). Importantly, this interpolation process did not alter the orientation distribution of the fibers within the stack.

To validate the geometry of the direct fiber model, we computed both the coronal and sagittal collagen fiber orientation distributions. For the coronal orientation distribution, we utilized the pixel-level PLM data obtained from the original image stack, taking into account the local "energy"

at each pixel. Similarly, for the sagittal orientation distribution, we summed up the PLM data obtained from the cropped block of the two sagittal sections (depicted in Figure 3B). Again, the energy weighting was applied to ensure accurate representation of the collagen fiber orientations in the sagittal plane.

2.3 Direct fiber modeling

2.3.1 Model construction

We constructed four models (Figure 4A) based on the procedure described previously (Ji et al. 2023a), corresponding to each sample listed in Table 2. Specifically, each modeled domain spanned 4.1 mm × 4.1 mm in-plane (radial and circumferential directions), and the through-thickness dimension varied by sample, ranging from 528 μm to 1168 μm, based on the number of 20 μm-thick coronal sections collected (as detailed in Table 2). Fibers were simulated using 3-dimensional linear truss elements (T3D2 in Abaqus). The locations of fibers were defined by sampling orientation values from PLM images at regularly spaced "seed" points (437 μm apart). Straight fibers, 13.68 μm in diameter, were traced at each seed point based on its orientation angle. The process was repeated for each layer, resulting in a stack of 2D layers with interpenetrating fibers. A conflict-resolution algorithm originally developed by Matuschke et al. (Matuschke et al. 2021; Matuschke et al. 2019) was employed to resolve fiber interpenetrations. This algorithm iteratively detected overlapping fiber elements and systematically shifted them apart along their minimal-separation directions until all overlaps were eliminated. Fiber elements were re-meshed to maintain lengths between 82μm and 164μm, while controlling the minimum radius of curvature for smoothness. The amplitudes of the fiber undulations in-depth were adjusted to more accurately represent the distribution of fibers in three dimensions.

To account for the natural curvature of the sclera, an additional step was performed to adjust the flat fiber model and match it to the curvature of the eyeball. The external radius of three sheep globes was manually measured, and the average radius was determined to be 14856 μm. The flat model was then projected onto a sphere with an external radius of 14856 μm, effectively introducing curvature to the model. It was important to note that this implied assuming that the sheep eye locally resembled a sphere.(Norman et al. 2010)

To assess the similarity between the model and the PLM images, the orientation distribution of the curved model was quantified and compared with the distribution obtained from the PLM images. This comparison aimed to evaluate how well the model captured the observed fiber orientations in the images. The quantification involved counting the occurrences of element

orientations within the model, where each element's orientation represented the slope angle in the section plane. This approach accounted for varying element sizes and enabled a proper comparison with the pixel-based measurements obtained from PLM. To evaluate the fitness of the orientation distributions, adjusted R-squared (adjusted R^2) values were employed (Miles 2005). The adjusted R^2 values provided a measure of how well the model's orientation distribution fits the distribution observed in the PLM images. The use of adjusted R^2 values allowed for the consideration of the complexity of the model and the number of parameters involved, providing a more robust evaluation metric than a conventional R^2.

In addition to the fiber model, a matrix model was also constructed (Figure 4B). In our model, compatibility was achieved geometrically and through consistent boundary conditions. Specifically, the matrix was designed to match the fiber model in dimensions and curvature, and fiber end-nodes were placed on the surfaces of the matrix. Both components were then subjected to the same displacement boundary conditions during simulation. This setup ensured kinematic compatibility between the fiber and matrix phases throughout the loading process.

2.3.2 Model inverse fitting

2.3.2.1 Meshing and material properties

Fibers were modeled as a hyperelastic Mooney-Rivlin material (Holzapfel 2001):

$$W = C_{10}(I_1 - 3) + C_{01}(I_2 - 3) + \frac{1}{D}(J - 1)^2 \quad (1)$$

where W was the strain energy density, C_{10} and C_{01} were the material constants to be determined by inverse fitting. Note that while it is common for both C_{10} and C_{01} to be positive in Mooney-Rivlin models, this is not a requirement. What matters is that the strain energy function remains positive definite (Weizel et al. 2022), i.e., $C_{10} + C_{01} > 0$. I_1 and I_2 were the first and second invariants of the right Cauchy-Green deformation tension, D determines the compressibility of the material and J was the determinant of the deformation gradient. The matrix was modeled as a neo-Hookean material with a shear modulus of 200 kPa (Coudrillier et al. 2015b; Girard et al. 2009b).

The fiber components were modeled using 3-dimensional linear truss elements (T3D2) in Abaqus. The length of the fiber elements ranged from 82 μm to 164 μm, resulting in aspect ratios between 6 and 12. The matrix was meshed using linear eight-noded hybrid hexahedral elements (C3D8H) in Abaqus, where the hybrid formulation introduces a pressure degree of freedom to enforce incompressibility. Accordingly, the parameter D was set to 0, which Abaqus interprets as full incompressibility and handles without numerical instability (Corp 2014). The element size for

the matrix varied among the samples due to differences in sample thickness, with 4 to 6 elements spanning the shell thickness. To ensure model accuracy, a mesh refinement study was conducted. The fiber model's mesh density was doubled, while the matrix model had its mesh density doubled in both in-plane directions and the thickness direction. The study's findings indicated that altering the mesh density had a negligible impact on stress predictions, with maximum stress values changing by less than 1%. Based on these findings, the chosen mesh density was deemed sufficient to ensure numerical accuracy in the obtained results.

2.3.2.2 Interactions

Fiber-fiber interactions were simulated in the following two ways. First, the interactions were considered by preventing fiber interpenetrations using Abaqus' general contact with no friction. Second, to enhance the interweaving effect of fibers and prevent them from sliding apart during stretching, a method involving the constraint of nodes was employed. Approximately 10% of the nodes, primarily located in the outer surface or boundary of the model, were selected. These nodes were connected to their closest neighboring nodes, and their relative motion in the Z direction was constrained to zero using linear constraint equations in Abaqus. By applying these constraints, the free ends of the fibers were better controlled, resulting in a more stable and realistic model.

Fiber-matrix interactions were ignored, as is usual in biomechanical models of the eyes (Grytz et al. 2014; Grytz and Meschke 2009; Petsche and Pinsky 2013). We recognize that in actual tissues there are interactions between the fibers and other fibers and the fibers and the matrix. Here it is important to point out that many conventional approaches to model soft tissues that use statistical and homogenization approaches disregard both interactions (Grytz et al. 2014; Grytz and Meschke 2009; Petsche and Pinsky 2013). Although our direct fiber modeling approach does not yet include detailed modeling of fiber-matrix interactions, it does account for fiber-fiber interactions and is therefore a step in the right direction.

2.3.2.3 Finite element analysis procedure

The fiber–matrix assembly was subjected to a quasi-static biaxial stretching process to replicate the experimental stress–strain data described in Section 2.1. Because mechanical interaction between the fiber and matrix domains was not modeled, the two components were treated as mechanically independent and solved separately using different finite element procedures. The matrix was modeled using the Abaqus standard implicit solver with C3D8H elements, suitable for simulating nearly incompressible soft tissue behavior. The fibers,

represented as T3D2 truss elements, were simulated using the explicit dynamic solver, which is more robust for resolving complex fiber–fiber contact interactions. The resulting stresses σ in the radial and circumferential directions were a combination of matrix and fiber contributions, with the matrix stress weighted by the fiber volume fraction (VF) as shown in Equation (2):

$$\sigma = (1 - \mathrm{VF})\sigma_{\mathrm{matrix}} + \mathrm{VF}\sigma_{\mathrm{fibers}} \quad (2)$$

To ensure efficient dynamic analysis, mass scaling was implemented, allowing for a stable time increment of 1e-5. The time step was selected to satisfy quasi-static loading conditions, whereas different values may be required to capture high-frequency dynamic responses. To confirm that the simulation remained quasi-static and that the mass scaling and time step did not introduce significant dynamic effects, the kinetic-to-internal energy ratio was monitored and remained below 5% (Supplemental data - Figure S5), a commonly accepted threshold for negligible inertial effects (Corp 2014).

2.3.2.4 Boundary conditions and inverse fitting procedure

In the biaxial stretching process of the fiber-matrix assembly (Figure 4C), a two-step approach was employed to simulate the experimental conditions. In the first step of the biaxial stretch simulation, radial and circumferential pre-stretching strains were applied to the model boundaries by prescribing displacements corresponding to those strain values as shown in Figure 4C. These pre-stretches represent the deformations caused by the 0.5g tare load in the physical experiments. Because these experimental strains were not directly measured, the radial and circumferential pre-stretch values were treated as unknowns and estimated through the inverse modeling procedure. Specifically, the inverse fitting algorithm adjusted these displacement boundary conditions (i.e., pre-stretching strains) in combination with the fiber material parameters to minimize the difference between the simulated and experimental stress-strain responses under equibiaxial loading. In the second step, the model was further stretched, and the same strains observed in the experiment were assigned as the displacement boundary condition to the fiber-matrix model. In this step, the model stress and strain values were recorded, starting from 0. This approach was consistent with the experimental setup, where the stress and strain resulting from the tare load were not included in the reported experimental stress-strain data. By applying this two-step biaxial stretch with the appropriate displacement boundary conditions, the model aimed to replicate the mechanical behavior observed in the experiment and allow for a comparison between the model's stress-strain behaviors and the experimental data.

During the inverse modeling procedure, there were four parameters to determine. The first two parameters were the pre-stretching strains along the radial and circumferential directions in the first step of the biaxial stretch. Since the resultant strains caused by the tare load were not characterized in the experiment, these values were unknown and needed to be determined through the inverse modeling process. The second two parameters were the material properties of the fibers (C_{10} and C_{01}).

In the inverse fitting procedure, two optimizations were performed to determine the optimal parameters and match the stress-strain data of the five loading protocols. In the first optimization, all four parameters (pre-stretching strains and fiber material properties) were optimized to match the stress-strain data obtained using loading protocol 1:1. Further discussion on the selection of loading protocol 1:1 can be found in the Discussion section. A simplex search method was used for this optimization (Lagarias et al. 1998). The algorithm aimed to find the values of the parameters that minimized the residual sum of squares (RSS) between the simulated and experimental stress-strain curves. The optimization process continued until the adjusted R^2 value between the curves exceeded 0.9, indicating a good fit between the model and experimental data. This optimization allowed for the determination of the optimal pre-stretching strains and fiber material properties (C_{10} and C_{01}).

In the second optimization, only the two pre-stretching strains were optimized, using the derived fiber material properties from the first optimization. This optimization aimed to match the stress-strain data obtained from the remaining four loading protocols. The same search method as before was employed, and the optimization was concluded when the adjusted R^2 value between the stress-strain curves exceeded 0.9 in both loading directions.

By performing these two optimizations, the model was able to find the optimal parameters that resulted in stress-strain curves closely aligned with the experimental data for all the five loading protocols.

Fiber material properties were obtained by matching experimental data from the equi-biaxial, 1:1, loading protocol. The natural question thus arises: to what extent would the results differ if the material properties were obtained by matching experimental data from other loading protocols? To address this, we selected one Sample, which had the best fitting accuracy using fiber material properties derived from the 1:1 loading protocol. We then independently derived the fiber material properties by fitting the experimental data from the 1:0.75, 0.75:1, and 1:0.5 loading protocols. The fitting process began with random initial values for the material properties, which were

iteratively optimized to match the experimental data. Importantly, each fitting process was conducted independently, without reference to results from other loading protocols.

To evaluate the physical significance and consistency of the derived fiber material properties, we focused on two key mechanical properties: the fiber elastic modulus and the shear bulk modulus. These properties are critical for understanding the mechanical behavior of the fibers under different loading conditions. The elastic modulus characterizes the stiffness of the fibers, while the shear bulk modulus reflects their resistance to shear deformation. Calculating these properties allowed us to assess whether the derived material properties were physically meaningful and consistent across different loading protocols.

The fiber elastic modulus was estimated by simulating uniaxial stretch of a single straight fiber using the optimal C10 and C01 values of the hyperelastic Mooney-Rivlin material. This approach provided a direct measure of the fiber's stiffness under tensile loading. The shear bulk modulus, on the other hand, was derived from the fitted material properties by analyzing the fiber's response to shear deformation. Both properties were calculated for each set of derived material properties obtained from the different loading protocols.

Preliminary analysis: During the preliminary analysis of the inverse fitting procedure using Sample #1, it was observed that the experimental data from loading protocol 0.5:1 exhibited negative strains along one loading direction. This suggested the presence of anisotropic mechanical properties, with one loading direction being much softer than the other direction. When assigning negative strains to the direct fiber model, it led to instability in the model. This was problematic because the direct fiber model is capable of accurately representing fiber tension, but not as well longitudinal fiber compression and buckling. As a result, all the loading protocols that showed negative strains were excluded from the analysis. Based on the mechanical testing results, the loading protocol 0.5:1 of all the samples presented negative strains (Supplemental data - Figure S1). Therefore, the results related to loading protocol 0.5:1 were not reported in this study. The focus was placed on the remaining loading protocols that did not exhibit negative strains.

3. Results

Figure 5 presents the fiber orientation distributions of the direct fiber model and corresponding PLM images for the four samples. The agreement between the model and PLM images was observed in both the coronal and sagittal planes. The alignment of these orientation curves yielded adjusted R^2 values exceeding 0.89 in all cases, indicating a strong match between the model and experimental data.

Figure 6 shows fiber displacements and stresses at full stretch of an example sample (Sample #4). Results for the other three samples are provided in the Supplementary Material (Figures S2–S4). The visualization revealed heterogeneous behaviors of the fibers, with varying deformations and stress distributions at the microscale. The model effectively captured the non-uniform response of the fibers under applied loading conditions, highlighting the intricate mechanical behavior within the tissue.

Isometric views of the Sample #4 direct fiber model during loading protocol 1:1 are shown in Figure 7. The visualization uses color to represent the maximum principal stress (left column) and displacement magnitudes (right column). Initially, the model showed curvature, which gradually flattened during stretching. As expected, more fibers experienced higher stress as stretching was applied, in a process of recruitment.

Stress-strain curves for all loading protocols, predicted by the optimized models using material parameters derived from the equi-biaxial loading protocol, are shown in Figure 8. These curves demonstrate decent agreement with experimental data in both the radial and circumferential directions for most loading protocol cases with R^2 values exceeded 0.85. Note that high values for the adjusted R^2, indicating a robust fit between the model predictions and experimental observations. The derived parameters that achieved this high level of agreement are provided in Table 3.

Figure 9 presents the fiber orientation distributions of the direct fiber model and the model's mechanical anisotropy at maximum strain state. The findings suggest that the stiffness along each direction is approximately proportional to the amount of fibers in the loading direction at the maximum strain state.

The derived fiber elastic and shear modulus demonstrated remarkable consistency across the results obtained from fitting different loading protocols of Sample #4, as shown in Figure 10. This

consistency underscores the robustness of our method and confirms that the derived material properties are largely independent of the choice of loading protocol used for fitting.

4. Discussion

Our goal was to continue advancing direct fiber models of soft tissues. Specifically, we aimed to conduct a more challenging test of the ability of the direct fiber modeling approach to capture sclera microstructure and anisotropic mechanics. We developed direct fiber models to simulate four sclera samples, incorporating specimen-specific 3D fiber architecture. Subsequently, we conducted an inverse fitting study and matched the models with specimen-specific anisotropic stress-strain behaviors from biaxial testing of the same samples. The study yielded two main findings. First, direct fiber model reconstruction can capture the 3D collagen structure of multiple sclera samples from different quadrants and eyes. Second, the macroscopic mechanical properties of the models matched with the experimental stress-strain data of the same sample obtained under various anisotropic loading conditions. Notably, this was achieved by having fit the models only to the equi-biaxial experiment. The derived material properties were then also shown to be appropriate for the other loading conditions. This indicates that the direct fiber models inherently incorporated the anisotropy of tissue mechanical behaviors within their fiber structure, thereby eliminating the necessity for separate optimization with different loading conditions. Below we discuss the findings in detail.

Finding 1. Direct fiber model reconstruction can capture the 3D collagen structure of multiple sclera samples from different quadrants and eyes.

In our previous study, the primary focus was on introducing the direct fiber modeling methodology, which involved utilizing experimental data from different samples and species obtained for other research purposes (Ji et al. 2023a). In this study we aimed to reconstruct and match the behavior of the same sample. To maintain the broad applicability, we chose to construct models of multiple sclera samples from different quadrants and eyes. This decision was driven by the fact that the collagen fiber architecture of the sclera varies both spatially between locations and between different eyes (Gogola et al. 2018b). Furthermore, it is known that the mechanical behavior of the sclera exhibits varying degrees of anisotropy across different quadrants (Coudrillier et al. 2013; Hua et al. 2022). By employing samples from both superior and temporal quadrants of multiple eyes, our study successfully demonstrated the robustness of the direct fiber model reconstruction approach in capturing the varying fiber structure. It is important to emphasize that our models were specimen-specific, meaning that the fiber structure was individually constructed based on each sample, and the model's behaviors were optimized using experimental data obtained from the same sample. Interestingly, the fiber orientation distributions obtained from the PLM data (red curves in Figure 5) are smoother than those derived from the

direct fiber models (green curves). This is because the PLM-based orientations sample actual tissues with a very large number of fibers, whose orientations are captured at pixel resolution and are subject to noise, whereas the model orientations are obtained from a much smaller set of fiber segments whose orientations are known with very high precision. Increasing the number of fiber segments would lead to smoother distributions, but at higher computational cost.

The morphological parameters used to construct the fiber models—specifically the fiber spacing (seeding density) and diameter—were selected based on a series of preliminary tests to achieve an appropriate balance between capturing collagen architecture, maintaining realistic tissue thickness, and ensuring computational feasibility. The seeding density directly influenced both the computational cost and the ability of the model to represent the underlying collagen architecture. A denser seeding of fibers provided a more accurate match to the orientation distributions derived from PLM images (as shown in Figure 5) but substantially increased the number of fibers and computational complexity. In contrast, sparse seeding reduced computational burden but risked losing key structural features. Fiber diameter, on the other hand, primarily impacted the model's thickness after resolving fiber–fiber interpenetrations. Larger fiber diameters necessitated greater shifts to resolve interpenetrations, which cumulatively led to an inflated tissue thickness relative to the original PLM-imaged block. Conversely, selecting a very small diameter reduced this effect but yielded unrealistically low fiber volume fractions and insufficient thickness. While PLM images can, in principle, resolve fiber dimensions, estimating diameter directly from them would require substantially denser sampling, further increasing computational demands. The parameters chosen in this study therefore reflect a deliberate compromise that enables realistic geometry, structural fidelity, and computational efficiency.

Finding 2: The macroscopic mechanical properties of the models matched with the experimental stress-strain data of the same sample obtained under various anisotropic loading conditions.

The importance of this finding is probably best understood when seen in the context of the conventional way that constitutive models of soft tissues are developed to incorporate fiber microstructure and nonlinear behavior. Prior studies have reported that a single equi-biaxial loading experiment is insufficient for predicting other loading responses (He and Lu 2022; Thomas et al. 2019; Zhang et al. 2019). To achieve the necessary predictive accuracy for other loading cases with uneven loading ratios, the equi-biaxial loading case must be supplemented with two additional loading conditions. Thus, for instance, the set of experimental tests used in this work

549 was developed and proven adequate to capture tissue properties using five experimental
550 conditions, three for model fitting and two for fit testing. This requirement indicates that the
551 conventional continuum models fail to capture at least part of the intrinsic anisotropy of the
552 microstructure, which must then be supplemented by more continuum parameters that require
553 other loading tests to fit. This complexity arises in large part because the nonlinear behavior of
554 collagenous tissues depends on fiber characteristics, including undulations across multiple
555 scales—with crimp representing a well-known small-scale periodic undulation observed in
556 collagen fibers (Islam et al. 2024; Jan and Sigal 2018; Lee et al. 2024) —as well as fiber-fiber
557 interactions (Wang et al. 2020). The conventional approach of capturing fiber architecture in an
558 element-by-element basis using one or more statistical distributions of fiber orientations (and
559 potentially other characteristics) has only a limited ability to describe the complexity of the tissue
560 microarchitecture. While techniques have been successfully implemented to account for fiber
561 crimp (Foong et al. 2023; Grytz et al. 2014; Grytz and Meschke 2009; Hill et al. 2012), the
562 approach is particularly limited in accounting for fiber-fiber interactions.

563 It is important to acknowledge that our direct fiber reconstruction approach still results in
564 an approximation of the actual fibrous structure of the sclera (more on this later in the subsection
565 on Limitations). Nevertheless, we argue that it represents a step forward for specimen-specific
566 modeling.

567 **Interpretation of the derived fiber material properties**

568 The “uniqueness” of so-called optimal parameters is a common concern in inverse fitting
569 techniques (Girard et al. 2009a; Zhou et al. 2019). To evaluate this, we conducted the inverse
570 fitting process using four different sets of starting parameters. While the derived fiber material
571 properties (C10 and C01) exhibited significant variation across the four samples, the estimated
572 fiber elastic modulus ranged from 0.47 GPa to 3.22 GPa for Samples #2, #3 and #4 (see Table
573 3). This range aligns with experimentally reported values in the literature: 0.2 GPa to 7 GPa for
574 bovine Achilles tendon fibers (van der Rijt et al. 2006; Yang et al. 2007), and 5 GPa to 11.5 GPa
575 in rat tail (Wenger et al. 2007). For Sample #1, the estimated fiber modulus was 23.97GPa , which
576 falls outside the experimentally reported ranges. This could be attributed to two potential factors.
577 First, the load may have been primarily borne by a small portion of the fibers, leading to an
578 overestimation of the fiber material properties. Second, the fiber volume fraction in our models
579 (approximately 15%) may not accurately represent the actual tissue composition. Experimental
580 data on scleral fiber volume fraction spans a wide range, from 18% to 93% (Boote et al. 2016;
581 Cone-Kimball et al. 2013; Edwards and Prausnitz 1998; Quigley et al. 1991). While there are

substantial variations between individual sclera, it is likely that a substantial contribution to the wide range is due to differences between methodologies, as we have discussed elsewhere (Wang et al. 2020). The derived fiber material properties are closely tied to the fiber volume fraction in the reconstructed models. However, reconstructing models with higher fiber density is challenging due to the increasing difficulty in tracing fibers and replicating their turns and undulations as the density increases (Yang et al. 2021). Further research is needed to comprehensively understand how variations in fiber volume fraction influence the behavior and derived material properties of the direct fiber model.

Another concern is whether the derived material properties and pre-stretching strains could lead to an overly favorable match between the models and experimental data across all loading protocols. To address this, we conducted a specific analysis using the fiber structure of Sample #1 and attempted to match the experimental data of Sample #2. While the model was able to capture the general stress-strain behavior of Sample #2 under the 1:1, 1:0.75, and 0.75:1 loading protocols using Sample #1's fiber architecture, it visibly failed to do so under the 1:0.5 protocol. This contrast highlights the importance of sample-specific fiber structure for accurate mechanical prediction (Figure 11). It is noted that the fitting accuracy for the 1:0.5 loading protocol in Sample #2 is not excellent, as evidenced by the single fitting result in Figure 8, which yielded an adjusted R^2 with 0.755 in the circumferential direction and 0.580 in the radial direction. However, the accuracy decreased to below 0.5 in the cross-fitting analysis. These results indicate that the model's applicability is not universal but depends on accurately matching the orientation distribution of the specific sample being studied. The relatively poor fitting accuracy for the 1:0.5 loading protocol further highlights the importance of sample-specific fiber orientation in replicating experimental data.

Strengths of direct fiber models

The models developed in this study have several strengths, some of which we have discussed above or elsewhere (Ji et al. 2023a). Briefly, the direct fiber models incorporate fiber interweaving and the resulting fiber-fiber interactions that play an important role in determining the structural stiffness of the sclera (Wang et al. 2020). The models also include collagen fibers of the sclera that are long and continuous. Thus, they can transfer forces over a long distance (Boote et al. 2020; Voorhees et al. 2018), that may also play important roles in tissue mechanics (Grytz et al. 2020; Huang et al. 2017; Islam et al. 2024; Lanir 2017). This is in contrast to the conventional continuum mechanics approaches where fibers exist only within a given element, disrupting load transmission at the element boundaries (He et al. 2024). Furthermore, the direct fiber models in

this work incorporate three-dimensional specimen-specific collagen architecture, whereas previous fiber-aware models tend to overlook or simplify the in-depth orientations of the collagen fibers (Coudrillier et al. 2013; Voorhees et al. 2017; Zhang et al. 2015). Collagen fiber variations in-depth of the tissue are crucial in determining the sclera's load-bearing capacity, particularly in bearing shear stresses, and may have clinical implications (Danford et al. 2013; Ji et al. 2023b).

The observed variability in sample thickness (Table 2) plays a structurally mediated role in influencing biomechanical behavior. In our experimental setup, stress was computed by normalizing force with the cross-sectional area, including measured thickness, ensuring that the reported stress–strain relationships reflected intrinsic material behavior rather than geometry-driven effects. However, the impact of thickness goes beyond geometry in our direct fiber modeling framework. Thicker samples contain a larger number of PLM-derived coronal sections, which leads to the inclusion of a broader range of fiber orientations through the depth of the tissue. This increased through-thickness heterogeneity in fiber directions can contribute to a more isotropic representation of collagen architecture. This phenomenon is evident in our results. Samples with greater thickness—specifically, Sample 2 (1168 μm) and Sample 4 (838 μm)—exhibited relatively isotropic mechanical and structural behavior (Figure 9), while the thinner samples, Sample 1 (888 μm) and Sample 3 (796 μm), showed more pronounced anisotropy. These observations suggest that sample thickness may influence apparent anisotropy through its role in shaping the depth-wise distribution of collagen fibers, which our modeling approach is specifically designed to capture.

In comparison to our previous studies, we implemented two improvements to the process of building direct fiber model structures. Firstly, we incorporated the natural curvature of the tissue into the model, enabling a more accurate representation of the physiological shape of the sclera. This enhancement ensured that the model mimicked more closely the three-dimensional geometry of the sclera, improving its fidelity. Secondly, we introduced a constraint function in Abaqus to deal with fibers that were not sufficiently constrained. This helped avoid, for example, cases where a fiber could be "pulled out" of the model. This function served to tightly constrain the interconnections between fibers. As a result, the model not only exhibited increased stability, but also better matched the actual interweaving and cohesion of collagen fibers in the sclera. This optimization helped overcome the challenge of inaccuracies caused by floating fibers and enhances the model's reliability and validity in representing the real tissue structure. We suspect that this constraint would not be necessary if we had modeled in more detail the fiber-fiber and fiber-matrix interactions. The simplifications we assumed on these interactions prevented

crossing and interpenetration, but nothing else. This allowed fibers much freedom to displace and slide. The roles of proteoglycans on this aspect of sclera behavior is important and still not well understood (Hatami-Marbini and Pachenari 2020; Murienne et al. 2015). It is also possible that our modeling of somewhat thick fiber bundles instead of small scale fibers may not have captured the full extent of the fiber entanglement that limits fiber sliding. Further work is necessary to characterize these aspects of the sclera and how to account for them accurately in models. Herein we just want to comment that we acknowledge that our treating of fiber-fiber and fiber-matrix interactions, while limited, is still more comprehensive than that in conventional continuum models where these are generally not only ignored but cannot be incorporated without cumbersome kludges. Our direct fiber modeling approach highlights the assumptions on the interactions and provides a platform for improving their modeling.

Limitations

The first limitation we would like to comment on was observed in the matching of stress-strain curves between the model and experimental data. While the majority of loading conditions exhibited strong agreement with adjusted R^2 values exceeding 0.9, there were instances, particularly in the loading protocol 1:0.5, where the model's fit was comparatively low. We do not know the cause, but this discrepancy may result from the sequential application of five different loading protocols during the testing process. After multiple rounds of testing at levels near the tissue limits, the tissue may have been affected. As a result, the model's behavior appeared to be stiffer than the corresponding experimental data in these cases. Future studies should either randomize the loading protocols or explicitly study the effects of protocol order. Despite this limitation, it is important to emphasize that the direct fiber modeling technique demonstrated robustness and effectiveness in capturing the overall mechanical behaviors of the sclera, as evidenced by the strong agreement between the model and experimental data in the majority of cases. The observed discrepancies in certain loading conditions provide valuable insights for future refinements of the model and highlight the need for further investigation into the dynamic changes in tissue properties during sequential loading.

Second, we encountered difficulties in accurately matching the loading protocol 0.5:1 due to the model's inability to perform well under compression. This limitation indicated that further optimization of the approach is required to enable stable simulations under compression. Again, we suspect that this is largely due to the simplifications in fiber-fiber interactions considered (Hatami-Marbini and Pachenari 2020; Murienne et al. 2015). Future efforts should be focused on addressing this issue to enhance the applicability of the direct fiber modeling approach.

Third, we used sheep eyes, and thus the question arises as to how well this would work with other tissues, or with other species. Considering the robustness of the approach in capturing the complex fiber structure and anisotropic mechanical behaviors of sheep sclera, we anticipated that the direct fiber modeling technique can serve as a valid and effective tool for investigating scleral biomechanics in other species and potentially in other collagen-based tissues as well. Tissues that approximate transverse isotropy, like the sclera, may fare better when imaged under PLM. More 3D isotropic tissues may require other imaging techniques. Future studies can extend the application of this approach to validate its broader utility and ensure its broad application across various tissues.

Fourth, only four samples were analyzed in this study. While the sample size was limited, the objective of the study was to validate the direct fiber modeling method using well-controlled, specimen-specific data, rather than to establish tissue characteristics across the population or other generalizations. These would likely require more samples. Whilst consistent performance across samples and loading protocols indicates method robustness, it should not be assumed that the method works equally well for other tissues.

Fifth, the direct fiber models, while consistent with experimentally measured fiber orientation distribution, are still approximations of the actual tissue. Several aspects were simplified or ignored in the modeling process, which may introduce discrepancies between the models and the real tissue. One such simplification was the assumption of uniform fiber or bundle diameters within the models. In reality, collagen fibers in the sclera exhibit variations in diameter (Gogola et al. 2018a; Jan et al. 2018; Komai and Ushiki 1991; Paidimarri et al. 2025). Additionally, sub-fiber level features were not explicitly included in the models, such as fiber crimp (Grytz et al. 2014; Lee et al. 2022). Future work would benefit from incorporating more detailed and realistic microstructural features, where the models can provide a more accurate representation of the scleral tissue and enhance our understanding of its mechanical behavior.

Six, the matrix mechanical properties were kept constant at literature values and not optimized iteratively like the fiber properties. This simplification was made for simplicity. Although the matrix properties could potentially affect fiber load-bearing and parameter fitting, their impact is considered minor. The fibers, being the primary load-bearing component, exhibit significantly greater stiffness compared to the matrix (Coudrillier et al. 2015a; Girard et al. 2009a). Analysis of our model indicated that the matrix bears only 4%–6% of the total reaction forces at the maximum strain. Therefore, we believe that the fiber properties dominate the model's behavior, while the matrix stiffness has minimal influence on the derived parameters. In future work, it would be

worthwhile to explore the role of matrix properties and consider more detailed matrix-fiber interactions for further refinement.

Seventh, we ignored fiber-matrix interactions that can be quite complex and have important effects on tissue behavior (Hatami-Marbini and Pachenari 2020; Murienne et al. 2016). While this is routinely done in continuum modeling of soft tissues, it is still a potentially important oversight. Interesting ideas have been proposed on how to deal with fiber-matrix interactions (Kakaletsis et al. 2023), but further research is needed to ensure that they do not overly constrain fiber behavior.

Eighth, in the current direct fiber model, we used T3D2 truss elements to represent collagen fibers. These elements support only axial loading (tension and compression) and neglect bending and torsional resistance. This modeling decision is justified by the slender geometry and tensile-dominated mechanics of collagen fibers, particularly under the planar biaxial loading conditions studied here. However, we acknowledge that excluding bending stiffness may limit the model's applicability in scenarios involving significant local curvature, compressive loads, or mechanical constraints that force fibers to reorient or buckle. Importantly, this limitation is not unique to our model: most statistical and homogenization-based approaches similarly neglect compression and buckling, often in even more simplified ways. Future extensions of our framework could incorporate beam elements or hybrid truss–beam formulations to enable more comprehensive modeling, especially for tissues subjected to complex geometries or loading environments.

It would be interesting in future work to compare between flat and curved models with identical microstructural inputs to elucidate the role of curvature in fiber recruitment, load distribution, and macroscopic anisotropy.

In conclusion, we performed a comprehensive and challenging test of the direct fiber modeling approach through the simulation of multiple sheep posterior sclera samples. We characterized the macroscopic and anisotropic stress-strain behaviors of the samples through biaxial mechanical testing. Then direct fiber models were generated based on the microstructural architecture of each sample. An inverse fitting process was employed to simulate biaxial stretching conditions, enabling the determination of optimal pre-stretching strains and fiber material properties. Our findings demonstrated the efficacy of the direct fiber modeling approach in simulating the scleral microarchitecture, capturing critical fiber characteristics, and accurately describing its anisotropic macroscale mechanical behaviors. Moreover, we highlighted the capability of the direct fiber models to inherently incorporate the anisotropy of tissue mechanical

745 behaviors within their fiber structure. Overall, the direct fiber modeling approach proved to be a
746 robust and effective tool for characterizing the biomechanics of sclera and other fibrous soft tissue.

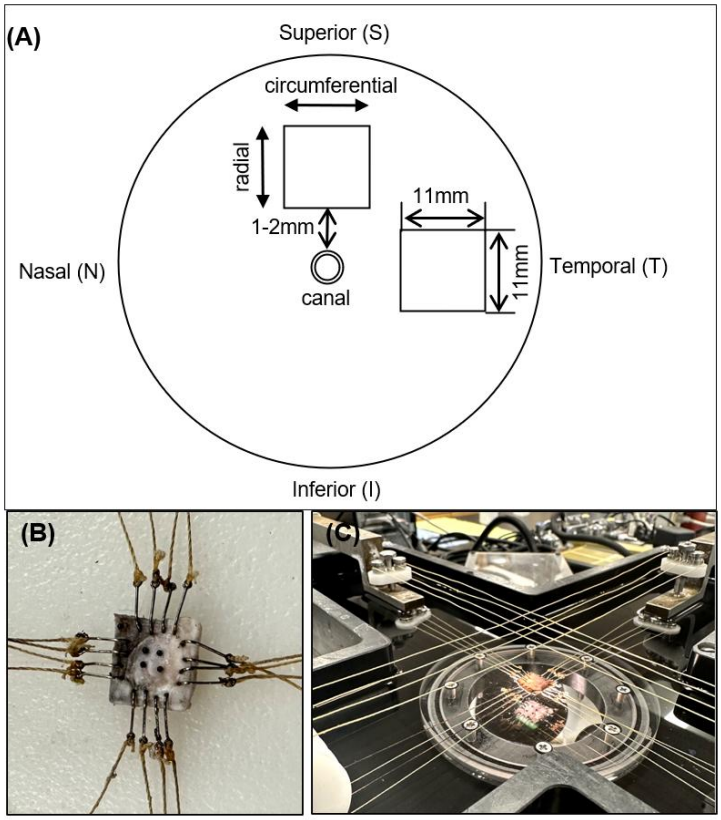

747

748 **Figure 1.** Key aspects of the experimental setup and procedures for the biaxial testing. (A)
749 Schematic diagram showcasing the posterior pole of the eye, highlighting the locations of the two
750 samples (depicted as yellow boxes) that were obtained specifically for the biaxial testing. Each
751 sample measured 11 mm × 11 mm in the in-plane dimensions. The corresponding sample
752 thicknesses are listed in Table 2. (B) An example image showing a sample with hooks attached,
753 ready for biaxial testing. The hooks ensured proper mounting and fixation of the sample during
754 the experimental procedures. (C) The sample was mounted on a custom-built biaxial mechanical
755 testing system, while continuously submerged in isotonic PBS solution. The loading axes of the
756 system were aligned with the circumferential and radial directions of the sample, ensuring precise
757 application of stress in the desired directions. The sample was then subjected to the five loading
758 protocols. Note that the crossed strings, as depicted at the lower right of the sample, were
759 corrected prior to conducting the experiment.

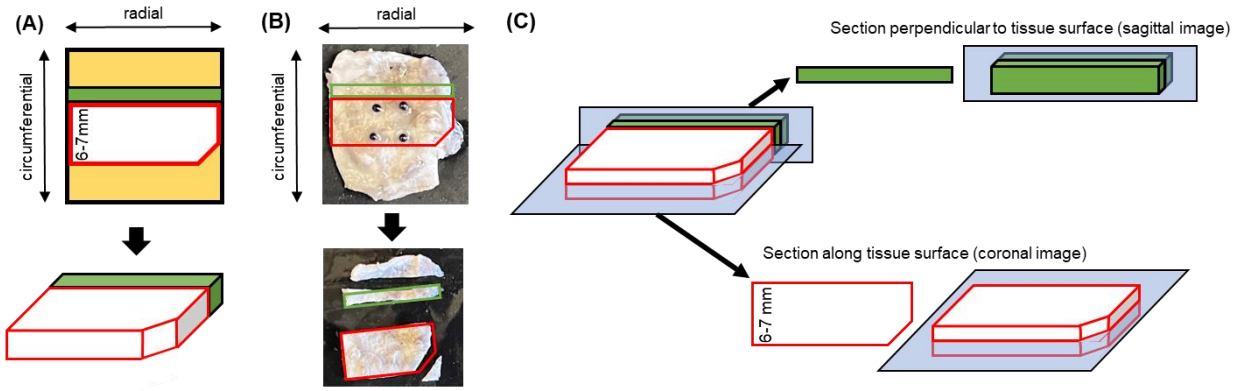

760

761 **Figure 2.** Process of sectioning a sclera sample. **(A)** Sclera sample after biaxial testing was
762 processed for sectioning (top: 2D view; bottom: 3D view of the region for sectioning). A notch at
763 the corner of the sample was used to indicate the tissue directions. Since it was not feasible to
764 section the same piece of tissue both coronally and sagittally, a sample (depicted as a white block,
765 the shorter length was 6-7mm) was obtained from the center of the tissue. Additionally, another
766 sample was acquired from the adjacent tissue next to the white block (shown as a green block).
767 **(B)** An example image of the sclera tissue with the two samples dissected. Prior to dissection, the
768 fiberglass markers attached to the tissue were carefully removed. **(C, top)** The green block was
769 sectioned sagittally, resulting in sagittal sections of the tissue. **(C, bottom)** The white block was
770 coronally sectioned, allowing for the acquisition of serial sections without any loss. The blue
771 surface depicted in the image represented the plane of sectioning.

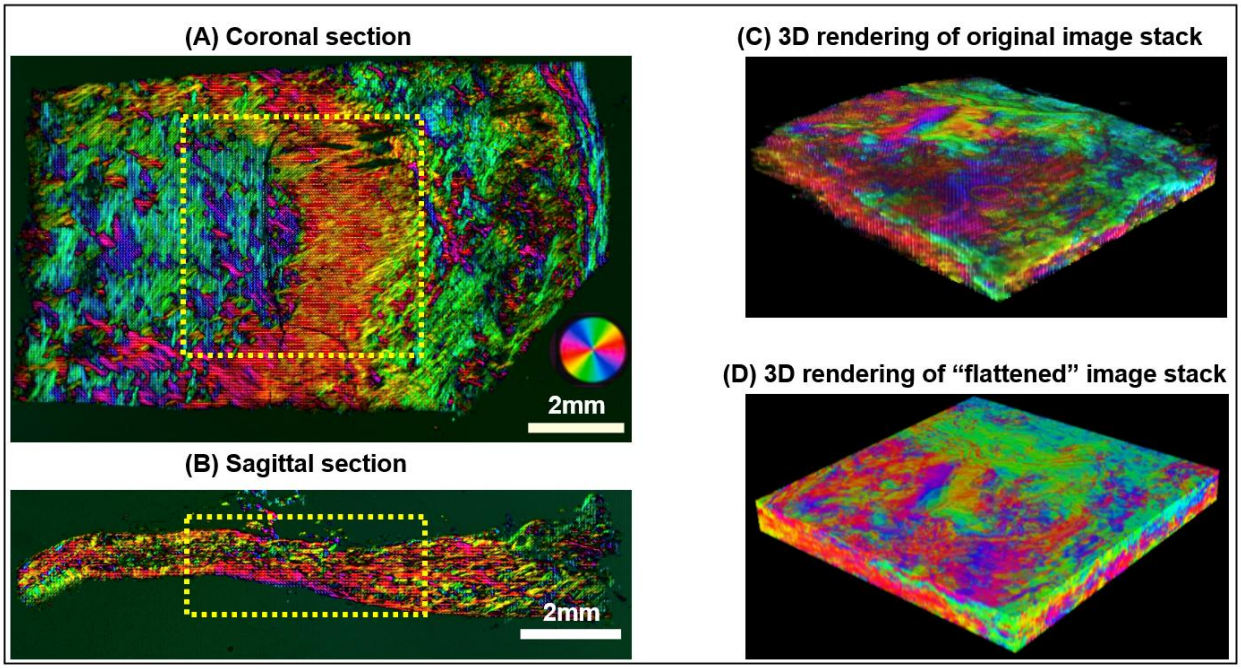

Figure 3. Example PLM images and process of image post-processing. **(A)** Example PLM image of a coronal section. A square-shape block was cropped from the stack and used as a reference to build the direct fiber model. **(B)** Example PLM image of a sagittal section. The model's in-depth fiber orientation distribution was adjusted based on the orientations obtained from the yellow block. The position of this block corresponded to the position of the square-shaped block obtained from the coronal section. The colors indicate the local fiber orientation in the section plane, with brightness proportional to the "energy" parameter. **(C)** The original stack showed irregular thickness from one location to another. **(D)** After interpolation, the thickness of the stack was uniformized which facilitates the tracing of fibers during the construction of the direct fiber model.

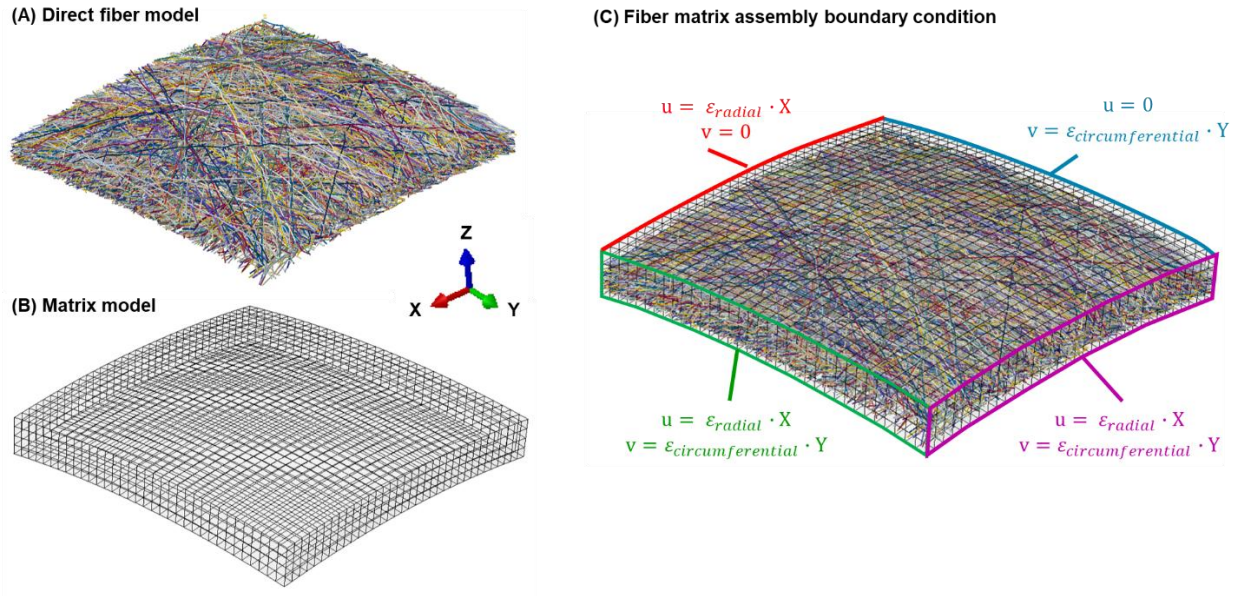

Figure 4. Isometric view of an example **(A)** direct fiber model and **(B)** matrix model. **(C)** Displacement boundary conditions were applied to the fiber matrix assembly, with components u, v representing displacement in X (radial) and Y (circumferential) direction, respectively. The displacement in Z direction was not constrained, given that fish hooks and strings did not restrict the sample's displacement in the Z direction. In the first step biaxial stretch, the value of ε_{radial} and $\varepsilon_{circumferential}$ were optimized and derived in the inverse fitting procedure. In the second step biaxial stretch, the experimental strain values were assigned to ε_{radial} and $\varepsilon_{circumferential}$, aiming to match the model with the stress-strain behaviors observed in the experimental data.

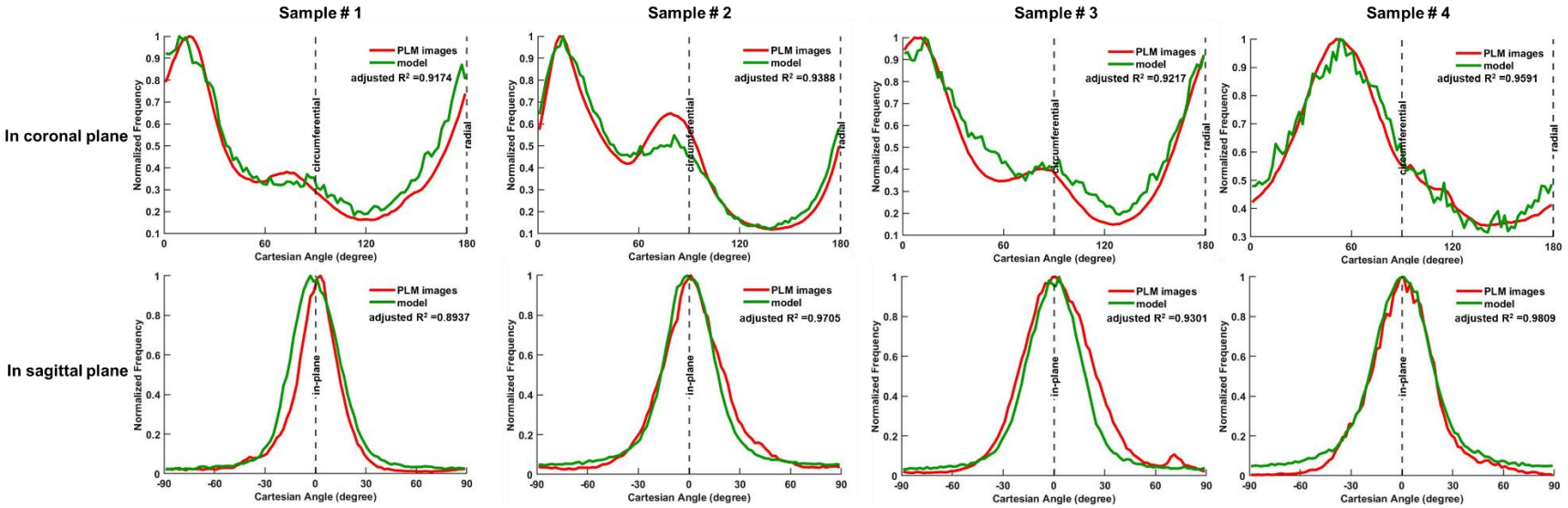

Figure 5. Fiber orientation distributions of the direct fiber model (green lines) and the corresponding PLM images (red lines). The analysis was performed in both the **(top row)** coronal and **(bottom row)** sagittal planes of the four samples. In the coronal plane, the PLM orientation was determined by analyzing a stack of all coronal images, with the radial direction represented by 0 and 180°, and the circumferential direction represented by 90°. The sagittal plane displayed the average orientation distribution obtained from two sections, with the in-plane direction represented by 0°. The frequencies of fiber orientations have been normalized by the total sum of frequencies for effective comparison. The results demonstrate a strong agreement between the fiber orientation distributions of the direct fiber model and those observed in the PLM images, in both the coronal and sagittal planes. All the adjusted R^2 values, which exceeded 0.89, indicate a high level of similarity between the model and experimental data.

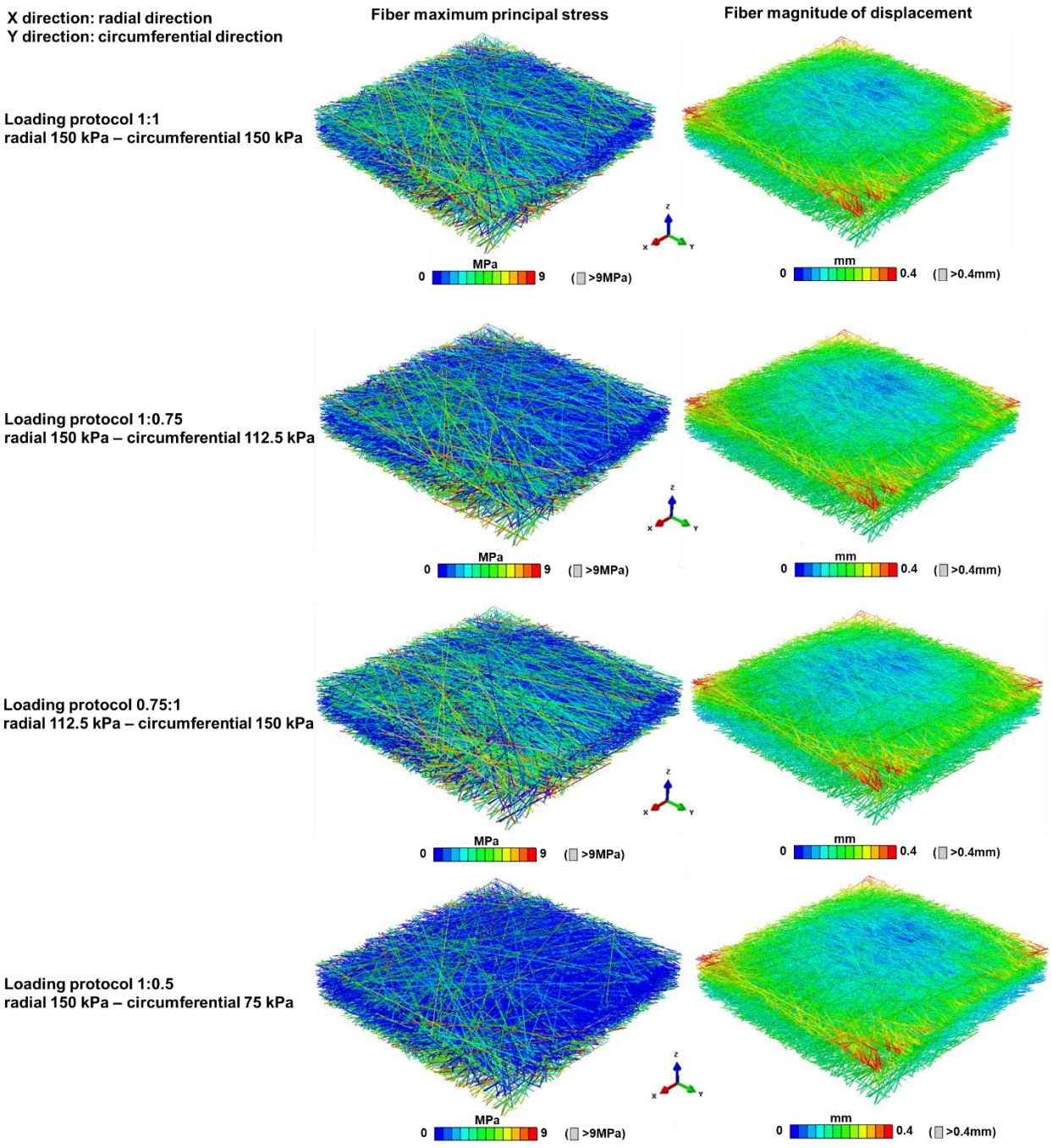

800

801 **Figure 6.** Isometric views of the direct fiber model of Sample #4 at full stretch. The visualization
802 was enhanced by coloring the fibers based on two important mechanical parameters: the
803 maximum principal stress (shown in the left column) and the magnitudes of displacement (shown
804 in the right column) for each loading protocol. The variations in stress and displacement patterns
805 can be observed, highlighting the non-uniform distribution of stresses and displacements within
806 the tissue.

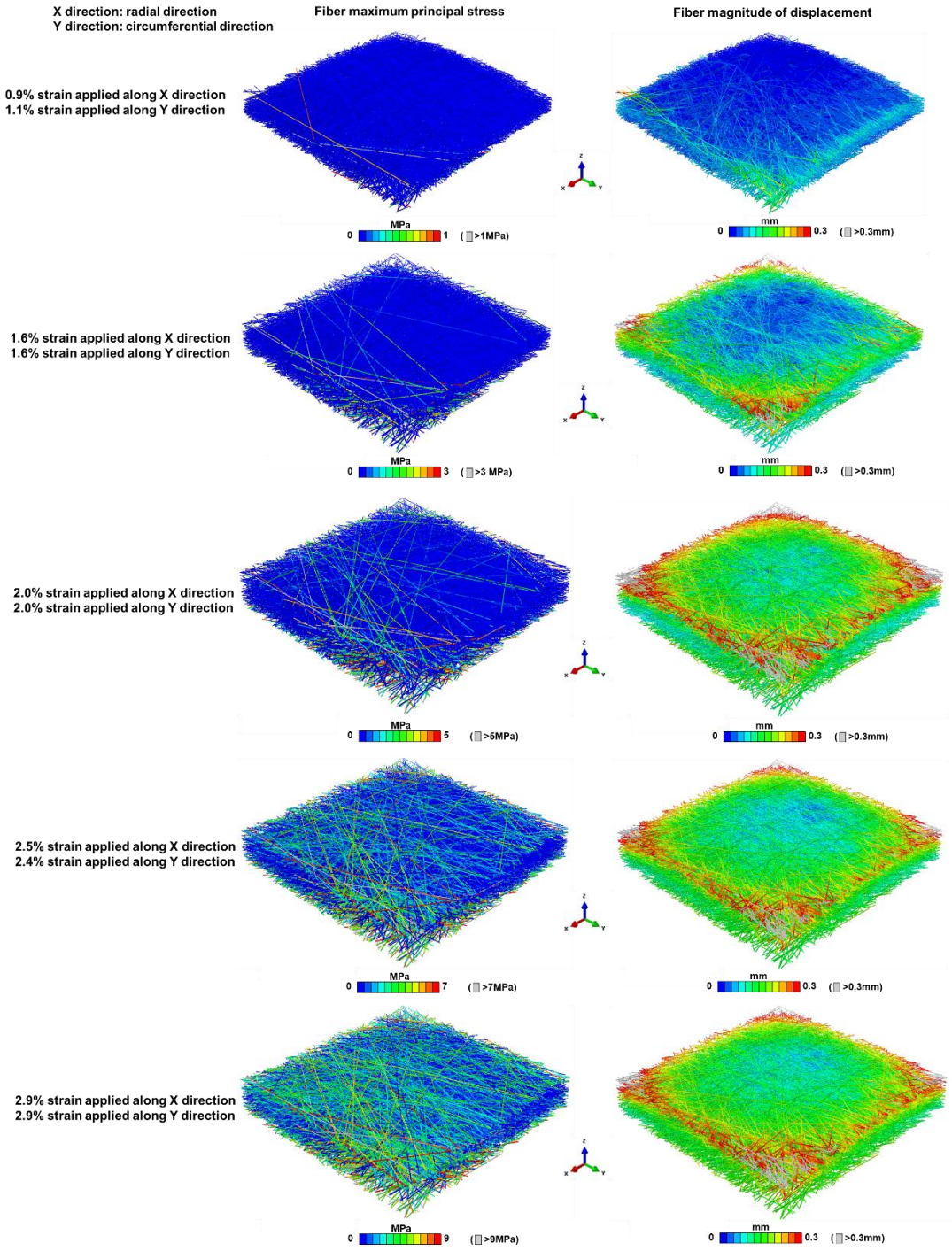

807

808 **Figure 7**. Isometric views of the direct fiber model of Sample #4 at different stages of the
809 simulation while undergoing loading protocol 1:1. The visualization was colored based on the
810 maximum principal stress (left column) and the magnitudes of displacement (right column). In the
811 early stage of the simulation, the model exhibited some curvature. As it underwent stretching, the

812 model gradually transformed into a flattened configuration. As stretching was applied, a larger
813 number of fibers experience higher levels of stress.

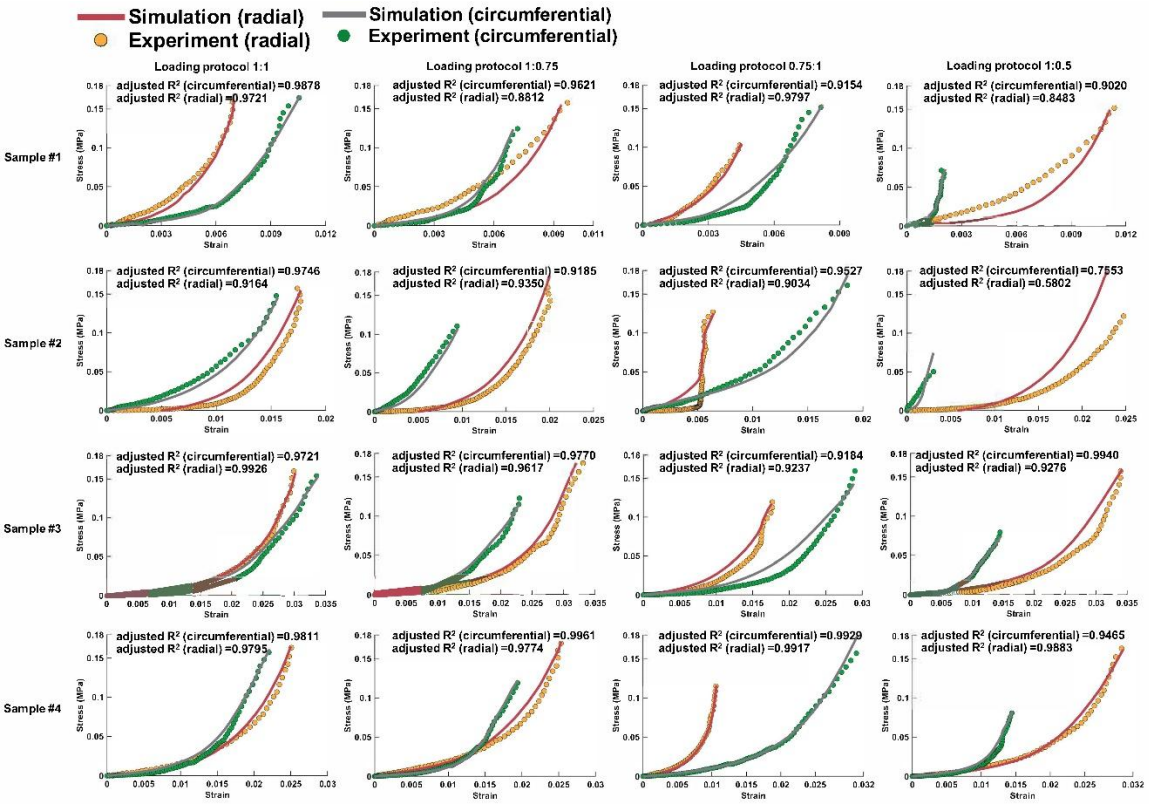

Figure 8. Stress-strain responses of the fiber-matrix assembly and the corresponding experimental data. The stress-strain curves were presented for both the radial and circumferential directions in each of the loading protocols. The fiber material properties were determined by fitting the model to the stress-strain data of loading protocol 1:1 (first column). These derived material parameters were directly used to predict the response of other loading protocols. The results demonstrated a successful fit between the model and the experimental data, with consistent agreement achieved simultaneously in both the radial and circumferential directions for each loading protocol. The goodness of fit was quantified using the adjusted R^2 value, which exceeded 0.9 in most of the cases. Notably for each sample, the stress-strain responses were obtained using the same fiber material properties throughout the simulations, with the variations observed solely in the pre-stretching strains.

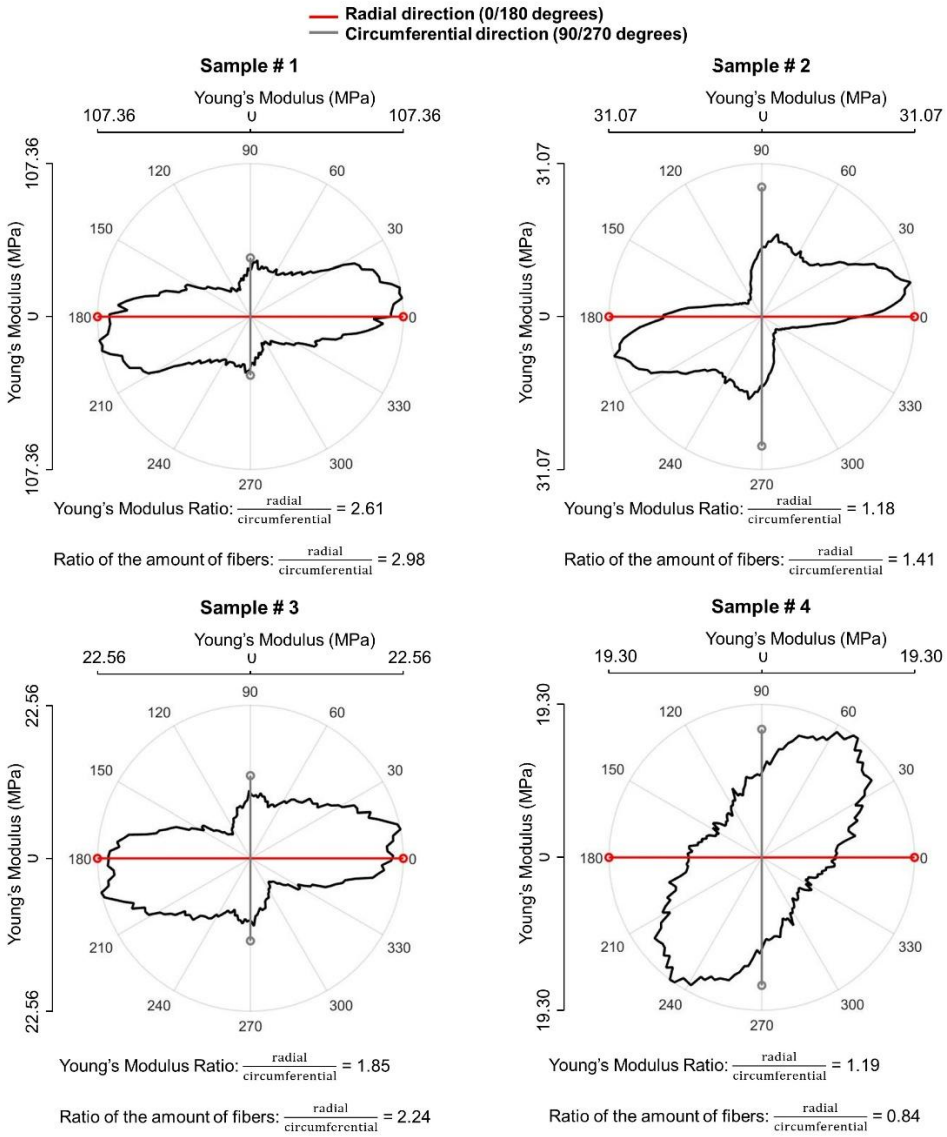

Figure 9. Orientation distribution and mechanical anisotropy of all the models. The orientation distributions are depicted in polar plots. The red and gray solid lines indicate the Young's moduli in the radial and circumferential directions, respectively, calculated from the slope of the model's stress–strain response at the maximum strain. All stiffness values are plotted using the same modulus scale for direct comparison. Below each plot, two anisotropy metrics are reported: 1) the Young's modulus ratio (radial/circumferential), representing mechanical anisotropy, and 2) the fiber amount ratio (radial/circumferential), representing structural anisotropy based on fiber count and orientation frequency (from Figure 5). The results show that while fiber architecture influences stiffness, the relationship is not strictly proportional, indicating other structural mechanisms may contribute to anisotropic behavior.

Loading protocol #	C_{10}	C_{01}	Pre-stretching strain (radial)	Pre-stretching strain (circumferential)	Fiber elastic modulus (GPa)	Fiber bulk modulus (GPa, $2(C_{10} + C_{01})$)
1:1	86.20	-0.049	0.0041	0.0074	0.512	0.172
1:0.75	97.601	-0.976	0.0045	0.005	0.574	0.193
0.75:1	77.729	-0.777	0.0135	0	0.457	0.154
1:0.5	86.625	-1.055	0.002	0.005	0.508	0.171

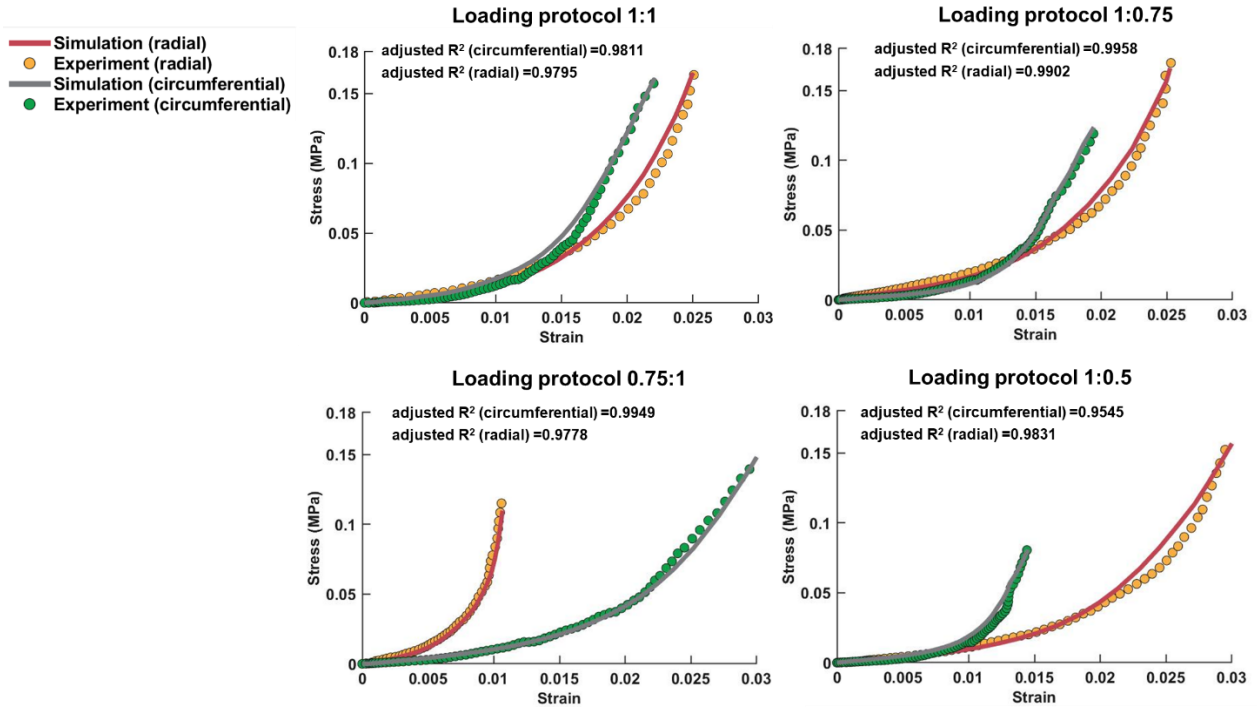

Figure 10. This figure illustrates the findings from the analysis using Sample #4 to assess the similarity of derived material properties when fitting the model to experimental data from different loading protocols. The table demonstrates that the values of C_{10} and C_{01} derived from fitting the model to different loading protocols are closely aligned, resulting in comparable fiber elastic modulus and fiber bulk modulus. Additionally, the stress-strain curves between the model and experimental data exhibit a strong overall fit, with an adjusted R^2 greater than 0.9. These results support the conclusion that the choice of loading protocol for fitting does not influence the derived fiber material properties.

Loading protocol #	C_{10}	C_{01}	Pre-stretching strain (radial)	Pre-stretching strain (circumferential)
1:1	581.35	-0.187	0.002	0.007
1:0.75			0.001	0.01
0.75:1			0.012	0.005
1:0.5			0	0

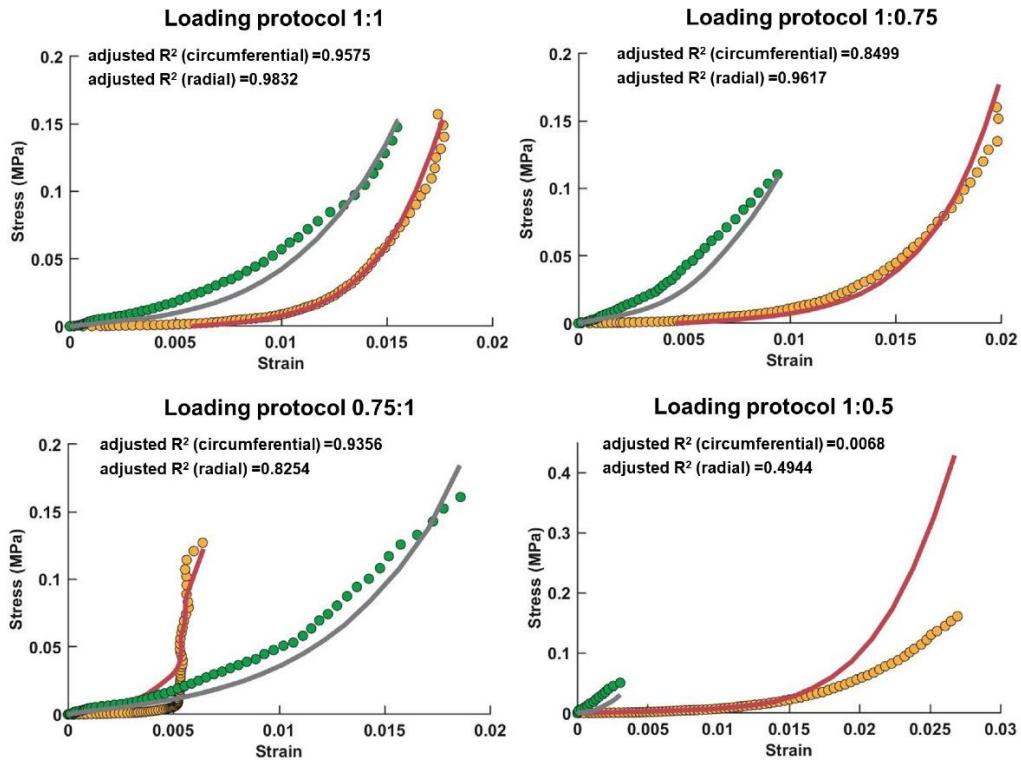

Figure 11. This figure presents the results of using the material parameters derived from Sample #1 to simulate the experimental stress-strain behavior of Sample #2, using Sample #2's fiber structure, aimed at assessing the possibility of achieving an overly favorable match between the models and experimental data. Following the process described in the main text, the fiber material properties C_{10} and C_{01} were derived by fitting the model to loading protocol 1:1. The results indicate successful matches between the model and experimental data for loading protocols 1:1, 1:0.75, and 0.75:1, with overall adjusted R^2 values exceeding 0.8. However, for loading protocol 1:0.5, the model exhibits softer behavior than the experiment in the circumferential direction and stiffer behavior in the radial direction, resulting in adjusted R^2 values lower than 0.5. As such, it cannot be considered as a valid match. These findings reinforce that the model's applicability is not universal but rather dependent on accurately matching the orientation distribution of the specific sample in order to replicate its experimental data.

Loading Protocol #	Radial (kPa)	Circumferential (kPa)
1:1	150	150
1:0.75	150	112.5
0.75:1	112.5	150
1:0.5	150	75
0.5:1	75	150

856 **Table 1.** Maximum radial (anterior-posterior) and circumferential (equatorial) stress values for
857 each biaxial loading protocol.

Sample #	Temporal/Superior	Sheep #	Thickness(μm)	Number of Coronal Sections
1	Superior	Eye-1	528	50
2	Temporal	Eye-2	1168	87
3	Superior	Eye-2	635	60
4	Temporal	Eye-3	838	74

Table 2. Information about the four posterior sclera samples used for direct fiber modeling. The samples were obtained from both the superior and temporal quadrants of three sheep eyes. Each sample had a different thickness, resulting in a variation in the number of collected coronal sections.

Sample #	Loading protocol #	C_{10}	C_{01}	Pre-stretching strain (radial)	Pre-stretching strain (circumferential)	Fiber elastic modulus (GPa)
1	1:1	4030	-2.0150	0.00825	0.00475	23.97
	1:0.75			0.00600	0.00725	
	0.75:1			0.00950	0.00750	
	1:0.5			0.00450	0.01050	
2	1:1	542.7	-0.1740	0.00050	0.00775	3.22
	1:0.75			0	0.01	
	0.75:1			0.01000	0.00625	
	1:0.5			0	0	
3	1:1	78.98	-0.058	0	0.00400	0.47
	1:0.75			0	0.01100	
	0.75:1			0.01	0.01000	
	1:0.5			0	0.01350	
4	1:1	86.20	-0.0485	0.00410	0.00740	0.51
	1:0.75			0.00600	0.00510	
	0.75:1			0.01300	0	
	1:0.5			0.00150	0.00550	

862 **Table 3.** The optimized fiber material properties (C_{10} and C_{01}) and the pre-stretching strains along radial and circumferential direction

Reference

Aghvami M, Billiar KL, Sander EA (2016) Fiber network models predict enhanced cell mechanosensing on fibrous gels Journal of biomechanical engineering 138:101006

Akima H (1970) A new method of interpolation and smooth curve fitting based on local procedures Journal of the ACM (JACM) 17:589-602

Akima H (1974) A method of bivariate interpolation and smooth surface fitting based on local procedures Communications of the ACM 17:18-20

Amini Khoiy K, Amini R (2016) On the biaxial mechanical response of porcine tricuspid valve leaflets Journal of biomechanical engineering 138:104504

Amini R, Barocas VH (2009) Anterior chamber angle opening during corneoscleral indentation: the mechanism of whole eye globe deformation and the importance of the limbus Investigative ophthalmology & visual science 50:5288-5294

Amini R, Voycheck CA, Debski RE (2014) A method for predicting collagen fiber realignment in non-planar tissue surfaces as applied to glenohumeral capsule during clinically relevant deformation Journal of Biomechanical Engineering 136:031003

Bellezza AJ, Hart RT, Burgoyne CF (2000) The optic nerve head as a biomechanical structure: initial finite element modeling Investigative ophthalmology & visual science 41:2991-3000

Bellini C, Glass P, Sitti M, Di Martino ES (2011) Biaxial mechanical modeling of the small intestine Journal of the mechanical behavior of biomedical materials 4:1727-1740

Bianco G, Girkin CA, Samuels BC, Fazio MA, Grytz R (2024) Biomechanical changes of tree shrew posterior sclera during experimental myopia, after retrobulbar vehicle injections, and crosslinking using genipin Scientific Reports 14:20667

Boote C et al. (2016) Changes in posterior scleral collagen microstructure in canine eyes with an ADAMTS10 mutation Molecular vision 22:503

Boote C, Sigal IA, Grytz R, Hua Y, Nguyen TD, Girard MJ (2020) Scleral structure and biomechanics Progress in retinal and eye research 74:100773

Chandran PL, Barocas VH (2006) Affine versus non-affine fibril kinematics in collagen networks: theoretical studies of network behavior

Chang Y, Li H, Huang S, He J, Yang S, Wang Q The Application of FFT Analysis on the Feeder Current Based on the Smooth Function in MATLAB. In: 2015 Asia-Pacific Energy Equipment Engineering Research Conference, 2015. Atlantis Press, pp 433-436

Clarin J, Dang D, Santos L, Amini R (2023) Mechanical characterization of porcine tricuspid valve anterior leaflets over time: applications to ex vivo studies ASME Open Journal of Engineering 2

Cone-Kimball E, Nguyen C, Oglesby EN, Pease ME, Steinhart MR, Quigley HA (2013) Scleral structural alterations associated with chronic experimental intraocular pressure elevation in mice Molecular vision 19:2023

Corp DSS (2014) ABAQUS Analysis User's Manual, Version 6.14.

Coudrillier B, Boote C, Quigley HA, Nguyen TD (2013) Scleral anisotropy and its effects on the mechanical response of the optic nerve head Biomech Model Mechanobiol 12:941-963 doi:10.1007/s10237-012-0455-y

Coudrillier B, Pijanka J, Jefferys J, Sorensen T, Quigley HA, Boote C, Nguyen TD (2015a) Collagen structure and mechanical properties of the human sclera: analysis for the effects of age J Biomech Eng 137:041006 doi:10.1115/1.4029430

Coudrillier B, Pijanka JK, Jefferys JL, Goel A, Quigley HA, Boote C, Nguyen TD (2015b) Glaucoma-related Changes in the Mechanical Properties and Collagen Micro-architecture of the Human Sclera PLoS One 10:e0131396 doi:10.1371/journal.pone.0131396

Coudrillier B, Tian J, Alexander S, Myers KM, Quigley HA, Nguyen TD (2012) Biomechanics of the human posterior sclera: age- and glaucoma-related changes measured using inflation testing Invest Ophthalmol Vis Sci 53:1714-1728 doi:10.1167/iovs.11-8009

Danford FL, Yan D, Dreier RA, Cahir TM, Girkin CA, Vande Geest JP (2013) Differences in the region- and depth-dependent microstructural organization in normal versus glaucomatous human posterior sclerae Invest Ophthalmol Vis Sci 54:7922-7932 doi:10.1167/iovs.13-12262

De Jesus AM, Aghvami M, Sander EA (2016) A combined in vitro imaging and multi-scale modeling system for studying the role of cell matrix interactions in cutaneous wound healing PloS one 11:e0148254

Edwards A, Prausnitz MR (1998) Fiber matrix model of sclera and corneal stroma for drug delivery to the eye AIChE journal 44:214-225

Ethier CR, Johnson M, Ruberti J (2004) Ocular biomechanics and biotransport Annu Rev Biomed Eng 6:249-273 doi:10.1146/annurev.bioeng.6.040803.140055

Fata B, Zhang W, Amini R, Sacks MS (2014) Insights into regional adaptations in the growing pulmonary artery using a meso-scale structural model: effects of ascending aorta impingement Journal of biomechanical engineering 136:021009

Feola AJ, Myers JG, Raykin J, Mulugeta L, Nelson ES, Samuels BC, Ethier CR (2016) Finite element modeling of factors influencing optic nerve head deformation due to intracranial pressure Investigative ophthalmology & visual science 57:1901-1911

Foong TY, Hua Y, Amini R, Sigal IA (2023) Who bears the load? IOP-induced collagen fiber recruitment over the corneoscleral shell Exp Eye Res 230:109446 doi:10.1016/j.exer.2023.109446

Geest JPV, Sacks MS, Vorp DA (2006) A planar biaxial constitutive relation for the luminal layer of intra-luminal thrombus in abdominal aortic aneurysms Journal of biomechanics 39:2347-2354

Girard MJ, Downs JC, Bottlang M, Burgoyne CF, Suh JK (2009a) Peripapillary and posterior scleral mechanics--part II: experimental and inverse finite element characterization J Biomech Eng 131:051012 doi:10.1115/1.3113683

Girard MJ, Downs JC, Burgoyne CF, Suh JK (2009b) Peripapillary and posterior scleral mechanics--part I: development of an anisotropic hyperelastic constitutive model J Biomech Eng 131:051011 doi:10.1115/1.3113682

Girard MJ et al. (2015) Translating ocular biomechanics into clinical practice: current state and future prospects Current eye research 40:1-18

Gogola A, Jan NJ, Brazile B, Lam P, Lathrop KL, Chan KC, Sigal IA (2018a) Spatial Patterns and Age-Related Changes of the Collagen Crimp in the Human Cornea and Sclera Invest Ophthalmol Vis Sci 59:2987-2998 doi:10.1167/iovs.17-23474

Gogola A, Jan NJ, Lathrop KL, Sigal IA (2018b) Radial and Circumferential Collagen Fibers Are a Feature of the Peripapillary Sclera of Human, Monkey, Pig, Cow, Goat, and Sheep Invest Ophthalmol Vis Sci 59:4763-4774 doi:10.1167/iovs.18-25025

Grytz R et al. (2014) Material properties of the posterior human sclera J Mech Behav Biomed Mater 29:602-617 doi:10.1016/j.jmbbm.2013.03.027

Grytz R, Meschke G (2009) Constitutive modeling of crimped collagen fibrils in soft tissues Journal of the Mechanical Behavior of Biomedical Materials 2:522-533 doi:https://doi.org/10.1016/j.jmbbm.2008.12.009

Grytz R, Yang H, Hua Y, Samuels BC, Sigal IA (2020) Connective Tissue Remodeling in Myopia and its Potential Role in Increasing Risk of Glaucoma Curr Opin Biomed Eng 15:40-50 doi:10.1016/j.cobme.2020.01.001

Hadi MF, Sander EA, Barocas VH (2012) Multiscale model predicts tissue-level failure from collagen fiber-level damage

Hatami-Marbini H, Pachenari M (2020) The contribution of sGAGs to stress-controlled tensile response of posterior porcine sclera PLoS One 15:e0227856 doi:10.1371/journal.pone.0227856

He X, Islam MR, Ji F, Wang B, Sigal IA (2024) Comparing continuum and direct fiber models of soft tissues: An ocular biomechanics example reveals that continuum models may artificially disrupt the strains at both the tissue and fiber levels Acta Biomaterialia 190:317-328

He X, Lu J (2022) Explicit consideration of fiber recruitment in vascular constitutive formulation using beta functions Journal of the Mechanics and Physics of Solids 163:104837

Hill MR, Duan X, Gibson GA, Watkins S, Robertson AM (2012) A theoretical and non-destructive experimental approach for direct inclusion of measured collagen orientation and recruitment into mechanical models of the artery wall J Biomech 45:762-771 doi:10.1016/j.jbiomech.2011.11.016

Holzapfel GA (2001) Biomechanics of soft tissue The handbook of materials behavior models 3:1049-1063

Hua Y, Salinas S, Quinn M, Ji F, Amini R, Sigal IA (2022) Mechanical anisotropy of the equatorial sclera does not concur with the primary collagen fiber orientations. Paper presented at the SB3C Summer Biomechanics, Biotransport and Bioengineering Conference, Eastern Shore, Maryland, June 20-23, 2022

Huang X, Zhou Q, Liu J, Zhao Y, Zhou W, Deng D (2017) 3D stochastic modeling, simulation and analysis of effective thermal conductivity in fibrous media Powder technology 320:397-404

Humphrey JD (2003) Continuum biomechanics of soft biological tissues Proceedings of the Royal Society of London Series A: Mathematical, Physical and Engineering Sciences 459:3-46

Islam MR, Ji F, Bansal M, Hua Y, Sigal IA (2024) Fibrous finite element modeling of the optic nerve head region Acta Biomater 175:123-137 doi:10.1016/j.actbio.2023.12.034

Jan NJ, Brazile BL, Hu D, Grube G, Wallace J, Gogola A, Sigal IA (2018) Crimp around the globe; patterns of collagen crimp across the corneoscleral shell Exp Eye Res 172:159-170 doi:10.1016/j.exer.2018.04.003

Jan NJ, Gomez C, Moed S, Voorhees AP, Schuman JS, Bilonick RA, Sigal IA (2017a) Microstructural Crimp of the Lamina Cribrosa and Peripapillary Sclera Collagen Fibers Invest Ophthalmol Vis Sci 58:3378-3388 doi:10.1167/iovs.17-21811

Jan NJ et al. (2015) Polarization microscopy for characterizing fiber orientation of ocular tissues Biomed Opt Express 6:4705-4718 doi:10.1364/BOE.6.004705

Jan NJ, Lathrop K, Sigal IA (2017b) Collagen Architecture of the Posterior Pole: High-Resolution Wide Field of View Visualization and Analysis Using Polarized Light Microscopy Invest Ophthalmol Vis Sci 58:735-744 doi:10.1167/iovs.16-20772

Jan NJ, Sigal IA (2018) Collagen fiber recruitment: A microstructural basis for the nonlinear response of the posterior pole of the eye to increases in intraocular pressure Acta Biomater 72:295-305 doi:10.1016/j.actbio.2018.03.026

Ji F et al. (2023a) A direct fiber approach to model sclera collagen architecture and biomechanics Exp Eye Res 232:109510 doi:10.1016/j.exer.2023.109510

Ji F, Quinn M, Hua Y, Lee PY, Sigal IA (2023b) 2D or not 2D? Mapping the in-depth inclination of the collagen fibers of the corneoscleral shell Exp Eye Res 237:109701 doi:10.1016/j.exer.2023.109701

Kakaletsis S, Lejeune E, Rausch M (2023) The mechanics of embedded fiber networks Journal of the Mechanics and Physics of Solids 181:105456 doi:https://doi.org/10.1016/j.jmps.2023.105456

Khoiy KA, Abdulhai S, Glenn IC, Ponsky TA, Amini R (2018a) Anisotropic and nonlinear biaxial mechanical response of porcine small bowel mesentery Journal of the mechanical behavior of biomedical materials 78:154-163

Khoiy KA, Pant AD, Amini R (2018b) Quantification of material constants for a phenomenological constitutive model of porcine tricuspid valve leaflets for simulation applications Journal of Biomechanical Engineering 140:094503

Kollech HG, Ayyalasomayajula A, Behkam R, Tamimi E, Furdella K, Drewry M, Vande Geest JP (2019) A Subdomain Method for Mapping the Heterogeneous Mechanical Properties of the Human Posterior Sclera Front Bioeng Biotechnol 7:129 doi:10.3389/fbioe.2019.00129

Komai Y, Ushiki T (1991) The three-dimensional organization of collagen fibrils in the human cornea and sclera Invest Ophthalmol Vis Sci 32:2244-2258

Lagarias JC, Reeds JA, Wright MH, Wright PE (1998) Convergence properties of the Nelder--Mead simplex method in low dimensions SIAM Journal on optimization 9:112-147

Lanir Y (1983) Constitutive equations for fibrous connective tissues Journal of biomechanics 16:1-12

Lanir Y (2017) Multi-scale structural modeling of soft tissues mechanics and mechanobiology Journal of Elasticity 129:7-48

Lee PY et al. (2024) Direct measurements of collagen fiber recruitment in the posterior pole of the eye Acta Biomater 173:135-147 doi:10.1016/j.actbio.2023.11.013

Lee PY, Yang B, Hua Y, Waxman S, Zhu Z, Ji F, Sigal IA (2022) Real-time imaging of optic nerve head collagen microstructure and biomechanics using instant polarized light microscopy Exp Eye Res 217:108967 doi:10.1016/j.exer.2022.108967

Mahutga RR, Barocas VH, Alford PW (2023) The non-affine fiber network solver: A multiscale fiber network material model for finite-element analysis Journal of the Mechanical Behavior of Biomedical Materials 144:105967

Matuschke F, Amunts K, Axer M (2021) fastPLI: A Fiber Architecture Simulation Toolbox for 3D-PLI Journal of Open Source Software 6:3042

Matuschke F, Ginsburger K, Poupon C, Amunts K, Axer M (2019) Dense fiber modeling for 3D-Polarized Light Imaging simulations Advances in parallel computing 34:240 - 253 doi:10.3233/APC190017

Midgett DE, Jefferys JL, Quigley HA, Nguyen TD (2020) The inflation response of the human lamina cribrosa and sclera: Analysis of deformation and interaction Acta Biomaterialia 106:225-241

Miles J (2005) R-squared, adjusted R-squared Encyclopedia of statistics in behavioral science

Moerman KM (2018) GIBBON: the geometry and image-based bioengineering add-on Journal of Open Source Software 3:506
Murienne BJ, Chen ML, Quigley HA, Nguyen TD (2016) The contribution of glycosaminoglycans to the mechanical behaviour of the posterior human sclera J R Soc Interface 13:20160367 doi:10.1098/rsif.2016.0367
Murienne BJ, Jefferys JL, Quigley HA, Nguyen TD (2015) The effects of glycosaminoglycan degradation on the mechanical behavior of the posterior porcine sclera Acta Biomater 12:195-206 doi:10.1016/j.actbio.2014.10.033
Newson T, El-Sheikh A (2006) Mathematical modeling of the biomechanics of the lamina cribrosa under elevated intraocular pressures Journal of biomechanical engineering 128:496-504
Nguyen TD, Ethier CR (2015) Biomechanical assessment in models of glaucomatous optic neuropathy Experimental eye research 141:125-138
Norman RE et al. (2010) Dimensions of the human sclera: Thickness measurement and regional changes with axial length Exp Eye Res 90:277-284 doi:10.1016/j.exer.2009.11.001
Paidimarri S, Arumugam B, Hung LF, Smith EL, 3rd, Burns AR, Ostrin LA (2025) Scleral ultrastructure in young rhesus monkeys: A stereological approach Vision Res 230:108592 doi:10.1016/j.visres.2025.108592
Pakzadmanesh M et al. (2024) Mechanically Induced Deformation of Nuclei in the Tricuspid Valve Interstitial Cells: Experimental Measurements and Multi-scale Computational Simulation ASME Open Journal of Engineering 3
Petsche SJ, Pinsky PM (2013) The role of 3-D collagen organization in stromal elasticity: a model based on X-ray diffraction data and second harmonic-generated images Biomech Model Mechanobiol 12:1101-1113 doi:10.1007/s10237-012-0466-8
Pijanka JK et al. (2012) Quantitative mapping of collagen fiber orientation in non-glaucoma and glaucoma posterior human sclerae Invest Ophthalmol Vis Sci 53:5258-5270 doi:10.1167/iovs.12-9705
Pijanka JK, Spang MT, Sorensen T, Liu J, Nguyen TD, Quigley HA, Boote C (2015) Depth-dependent changes in collagen organization in the human peripapillary sclera PLoS One 10:e0118648 doi:10.1371/journal.pone.0118648
Preibisch S, Saalfeld S, Tomancak P (2009) Globally optimal stitching of tiled 3D microscopic image acquisitions Bioinformatics 25:1463-1465 doi:10.1093/bioinformatics/btp184
Quigley HA, Dorman-Pease ME, Brown AE (1991) Quantitative study of collagen and elastin of the optic nerve head and sclera in human and experimental monkey glaucoma Current eye research 10:877-888
Rada JA, Shelton S, Norton TT (2006) The sclera and myopia Exp Eye Res 82:185-200 doi:10.1016/j.exer.2005.08.009
Raghupathy R, Barocas VH (2009) A closed-form structural model of planar fibrous tissue mechanics Journal of biomechanics 42:1424-1428
Roberts CJ, Liu J (2017) Corneal Biomechanics: from theory to practice. Kugler Publications,
Salinas SD, Clark MM, Amini R (2019) Mechanical response changes in porcine tricuspid valve anterior leaflet under osmotic-induced swelling Bioengineering 6:70
Salinas SD, Clark MM, Amini R (2020) The effects of -80 degrees C short-term storage on the mechanical response of tricuspid valve leaflets J Biomech 98:109462 doi:10.1016/j.jbiomech.2019.109462

Salinas SD, Farra YM, Amini Khoiy K, Houston J, Lee C-H, Bellini C, Amini R (2022) The role of elastin on the mechanical properties of the anterior leaflet in porcine tricuspid valves Plos one 17:e0267131

Schindelin J et al. (2012) Fiji: an open-source platform for biological-image analysis Nat Methods 9:676-682 doi:10.1038/nmeth.2019

Stylianopoulos T, Barocas VH (2007) Volume-averaging theory for the study of the mechanics of collagen networks Computer methods in applied mechanics and engineering 196:2981-2990

Taber LA (2009) Towards a unified theory for morphomechanics Philosophical transactions of the royal society a: mathematical, physical and engineering sciences 367:3555-3583

Thomas VS, Lai V, Amini R (2019) A computational multi-scale approach to investigate mechanically-induced changes in tricuspid valve anterior leaflet microstructure Acta Biomater 94:524-535 doi:10.1016/j.actbio.2019.05.074

Tran H et al. (2017) Formalin Fixation and Cryosectioning Cause Only Minimal Changes in Shape or Size of Ocular Tissues Sci Rep 7:12065 doi:10.1038/s41598-017-12006-1

van der Rijt JA, van der Werf KO, Bennink ML, Dijkstra PJ, Feijen J (2006) Micromechanical testing of individual collagen fibrils Macromol Biosci 6:697-702 doi:10.1002/mabi.200600063

Voorhees AP, Jan NJ, Hua Y, Yang B, Sigal IA (2018) Peripapillary sclera architecture revisited: A tangential fiber model and its biomechanical implications Acta Biomater 79:113-122 doi:10.1016/j.actbio.2018.08.020

Voorhees AP, Jan NJ, Sigal IA (2017) Effects of collagen microstructure and material properties on the deformation of the neural tissues of the lamina cribrosa Acta Biomater 58:278-290 doi:10.1016/j.actbio.2017.05.042

Wang B, Hua Y, Brazile BL, Yang B, Sigal IA (2020) Collagen fiber interweaving is central to sclera stiffness Acta Biomater 113:429-437 doi:10.1016/j.actbio.2020.06.026

Weizel A et al. (2022) Hyperelastic parameter identification of human articular cartilage and substitute materials Journal of the Mechanical Behavior of Biomedical Materials 133:105292

Wenger MP, Bozec L, Horton MA, Mesquida P (2007) Mechanical properties of collagen fibrils Biophys J 93:1255-1263 doi:10.1529/biophysj.106.103192

Whitford C, Joda A, Jones S, Bao F, Rama P, Elsheikh A (2016) Ex vivo testing of intact eye globes under inflation conditions to determine regional variation of mechanical stiffness Eye Vis (Lond) 3:21 doi:10.1186/s40662-016-0052-8

Yang B, Jan NJ, Brazile B, Voorhees A, Lathrop KL, Sigal IA (2018) Polarized light microscopy for 3-dimensional mapping of collagen fiber architecture in ocular tissues J Biophotonics 11:e201700356 doi:10.1002/jbio.201700356

Yang B et al. (2021) Instant polarized light microscopy for imaging collagen microarchitecture and dynamics J Biophotonics 14:e202000326 doi:10.1002/jbio.202000326

Yang L, van der Werf KO, Koopman BF, Subramaniam V, Bennink ML, Dijkstra PJ, Feijen J (2007) Micromechanical bending of single collagen fibrils using atomic force microscopy J Biomed Mater Res A 82:160-168 doi:10.1002/jbm.a.31127

Zhang L, Albon J, Jones H, Gouget CL, Ethier CR, Goh JC, Girard MJ (2015) Collagen microstructural factors influencing optic nerve head biomechanics Invest Ophthalmol Vis Sci 56:2031-2042 doi:10.1167/iovs.14-15734

Zhang W, Ayoub S, Liao J, Sacks MS (2016) A meso-scale layer-specific structural constitutive model of the mitral heart valve leaflets Acta biomaterialia 32:238-255

Zhang W, Zakerzadeh R, Zhang W, Sacks MS (2019) A material modeling approach for the effective response of planar soft tissues for efficient computational simulations Journal of the mechanical behavior of biomedical materials 89:168-198

Zhou D, Abass A, Eliasy A, Studer HP, Movchan A, Movchan N, Elsheikh A (2019) Microstructure-based numerical simulation of the mechanical behaviour of ocular tissue J R Soc Interface 16:20180685 doi:10.1098/rsif.2018.0685